1 **Histone deacetylase 6 inhibition promotes microtubule acetylation and facilitates**
2 **autophagosome-lysosome fusion in dystrophin-deficient *mdx* mice**

3 Akanksha Agrawal[1], Erin L. Clayton[1], Courtney L. Cavazos[1], Benjamin A. Clayton[1],

4 George G. Rodney[1*]

5 1. Department of Integrative Physiology, Baylor College of Medicine, Houston, TX, USA
6
7 [*]All correspondence should be sent to rodney@bcm.edu

8 **Abstract**

9 Duchenne Muscular Dystrophy (DMD) is a severe X-linked genetic disorder. Defective autophagy

10 and disorganized microtubule network contributes to DMD pathogenesis, yet the mechanisms by

11 which microtubule alterations regulate autophagy remain elusive. We show decreased acetylated

12 α-tubulin and enhanced histone deacetylase (HDAC6) expression in *mdx* mice. Pharmacological

13 inhibition of HDAC6 increases tubulin acetylation and enhances Q-SNARE complex formation,

14 leading to improved autophagosome-lysosome fusion. HDAC6 inhibition reduces apoptosis,

15 inflammation, muscle damage and prevents contraction induced force loss. HDAC6 inhibition

16 restores peroxiredoxin (PrxII) by increasing its acetylation and protecting it from hyper-oxidation,

17 hence modulating intracellular redox status in *mdx* mice. Genetic inhibition of Nox2 activity in

18 *mdx* mice promotes autophagosome maturation. Our data highlight that autophagy is differentially

19 regulated by redox and acetylation in *mdx* mice. By restoring tubulin acetylation HDAC6

20 inhibition enhances autophagy, ameliorates the dystrophic phenotype and improves muscle

21 function, suggesting a potential therapeutic target for treating DMD.

22 **Introduction**

23 Duchenne Muscular Dystrophy (DMD) is the X-linked recessive genetic disorder caused by

24 mutations in *DMD* gene which encodes for dystrophin (Dp427m), a key component of the

25   dystrophin-glycoprotein complex (DGC). It affects approximately 1:4000 to 1:5000 live male

26   births worldwide [1] resulting in progressive muscle wasting and degeneration, leading to death due

27   to cardiac dysfunction and respiratory failure [2]. Over the past two decades, several therapeutic

28   approaches have been evaluated to combat the pathogenesis of the disease, but DMD is still

29   incurable. Novel genetic approaches hold promising therapy; [3] however, many challenges still

30   exist due to the variability in exon skipping efficiency among patients, the non-homogenous

31   restoration of dystrophin between muscle types (including absence of effect of current exon

32   skipping agents on cardiac muscle), and minimal alterations in immune cell infiltration. In order

33   to combat these limitations, the treatment plan for DMD will likely entail a combination of genetic

34   and pharmacological interventions.

35   Dystrophin is a large cytoskeletal protein located at the sarcolemma that mechanically links the

36   internal cytoskeleton to the extracellular matrix and is critical for muscle-membrane stability

37   during contraction [4]. Lack of dystrophin results in disassembly of the DGC and increases the

38   sarcolemma susceptibility to contraction-induced injury [5]. This leads to a series of pathological

39   events including, increased ROS signaling, aberrant Ca^{2+} release, inflammation, impaired

40   autophagy, fibrosis, apoptosis, and decreased force production. [5, 6, 7]

41   Macroautophagy, hereafter referred to as autophagy, is a highly conserved process involving a

42   series of sequential events for bulk degradation of cytosolic components and organelles through

43   delivery of autophagosomes to lysosomes, and thus, maintaining cellular homeostasis.[8]

44   Accumulating evidence shows that impaired autophagy contributes to muscle weakness and cell

45   death in both *mdx* mice (mouse model of DMD) and DMD patients [9, 10]. Recent work from our lab

46   has shown that Nox2/Src kinase impairs autophagy by regulating the PI3K/Akt/mTOR pathway

47   in *mdx* mice [7]. To better comprehend how defective autophagy leads to DMD pathophysiology,

2

48   and to develop therapeutic strategies, we need to elucidate the defects at different steps of the

49   autophagic pathway.

50   Dystrophin is a microtubule-associated protein found to bind microtubules (MT). [11] The MT lattice

51   becomes disorganized when dystrophin expression is ablated as in the *mdx* mouse [11, 12, 13]. We have

52   shown that the increased Nox2-ROS observed in *mdx* skeletal muscle regulates the MT network[14].

53   MTs undergo post-translational modifications that regulate their biological functions. Some

54   studies suggest detyrosination of α-tubulin increases muscle stiffness and decreases force

55   production in *mdx* mice [15, 16]. In non-muscle cells, acetylation of α-tubulin has been shown to

56   regulate the formation of pre-autophagosomal structures, vesicular movements and

57   autophagosome-lysosome fusion [17, 18, 19]. Acetylated MTs recruit the motor protein kinesin-1 to

58   transport autophagosomes in a cargo-specific manner along the MT tracks. Changes in MT

59   acetylation leads to alterations in MT dynamics and organization, cell migration, and autophagy[18,

60   20]. Despite the extensive investigations largely based on MT dynamics, stability and its altered

61   network in dystrophic mice, no study has addressed the role of acetylated MTs specifically on

62   autophagosome biogenesis and autophagosome-lysosome fusion in DMD. Therefore, the present

63   study was designed to unravel the plausible mechanisms underpinning the role of MTs in

64   regulating autophagy in dystrophic mice.

65   Histone deacetylases (HDACs) are a class of deacetylase enzymes involved in chromatin

66   remodeling and gene expression [21]. Currently, epigenetic drugs (e.g. Givinostat) targeting HDACs

67   are in phase III clinical trials to assess their functional effects in DMD patients [2, 22]. Recently,

68   HDAC6 (Class IIb) inhibition has emerged as one potential selective pharmacological target in

69   neurodegenerative diseases. HDAC6 catalyzes the deacetylation of non-histone proteins such as

70   α-tubulin, leading to altered MT stability and organization [23]. In addition, HDAC6 can control

3

71 redox regulation through acetylation of peroxiredoxin (Prx1 and PrxII)[24, 25]. Therefore, selective

72 HDAC6 inhibition has the potential to reduce the toxicity related to the off-target effects of pan-

73 HDAC inhibitors (Givinostat). [26] Recent investigations have suggested that the HDAC6 inhibitor,

74 Tubastatin A (TubA) promotes MT acetylation, improving autophagic flux, redox balance, and

75 functional recovery in neurodegenerative disorders [19, 27, 28, 29], cardiomyopathy [30], idiopathic

76 pulmonary fibrosis[31], myocardial ischemia/reperfusion injury [32], osteoarthritis [33], and kidney injury

77 [34]. In the current study, we show differential regulation of autophagy in *mdx* skeletal muscle; while

78 autophagosome maturation is regulated by Nox2-ROS, autophagosome-lysosome fusion is

79 regulated by MT acetylation. Furthermore, we discovered the therapeutic efficacy of HDAC6

80 inhibitor, TubA, in promoting MT acetylation and restoring autophagic flux in *mdx* mice. TubA

81 treatment significantly restricted muscle damage and apoptosis and induced muscle functional

82 recovery.

83 **Results:**

84 **Impaired autophagosomal biogenesis/maturation in *mdx* mice**

85 The maturation of double-membrane vesicle structures called autophagosomes occurs in a highly

86 orchestrated manner to achieve successful delivery to the lysosomes for fusion [35]. One of the initial

87 steps in autophagosome biogenesis is the recruitment and activation of the class III

88 phosphatidylinositol 3-kinase complex (PI3K), consisting of Beclin, ATG14L, VPS34, and VPS15

89 to facilitate the phagophore nucleation[36]. Immunoblot analyses of TA muscle homogenate revealed

90 a significant decrease in ATG14L and VPS34, whereas both Beclin and VPS15 were found to be

91 increased in *mdx* muscles as compared to WT **(Fig.1a-b).** Immunoprecipitation of Beclin followed

92 by western blot for ATG14L showed decreased ATG14L/Beclin complex formation in *mdx* muscle

93 as compared to WT while Bcl-2/Beclin complex formation was not altered **(Fig. 1c).** These data

4

94   are consistent with inhibition of vesicle nucleation in *mdx* mice**.** Autophagy induction by

95   heterodimerization of Beclin with ATG14L-VPS34 is regulated by activated JNK. JNK-

96   interacting protein 1 (JIP-1) binds protein kinases (e.g. MAPKK/MKK7) to promote

97   phosphorylation and activation of JNK [37]. We observed that the protein expressions levels of JIP-

98   1 and p-JNK (Thr183/Ty185) are downregulated in *mdx* skeletal muscle, whereas MAPKK was

99   significantly upregulated in *mdx* mice **(Fig 1d-e).** P-JNK phosphorylates Bcl-2 (S70), which

100   disrupts the Bcl-2/Beclin complex, allowing Beclin to bind the PI3KclassIII complex for

101   phagophore nucleation. We found lower levels of p-Bcl-2 in *mdx* muscles as compared to WT,

102   likely due to the decrease in p-JNK levels **(Fig 1d-e).** Together, these observations suggest that

103   phagophore nucleation is disrupted due to inhibition of JIP-1/JNK activation and subsequent

104   phosphorylation of Bcl-2 in *mdx* mice.

105   Vesicle nucleation is followed by elongation and expansion of the phagophore in the cytoplasm,

106   which is regulated by the ATG5-12 complex. Our data revealed that WIPI-1 (WD Repeat Domain

107   Phosphoinositide Interacting 1), an early marker of autophagosome formation which fosters the

108   recruitment of downstream ATGs, was significantly downregulated in *mdx* muscle **(Fig. 1f-g)**

109   whereas ATG7, ATG4B, and ATG5-12 did not show any prominent change in *mdx* as compared

110   to WT **(Fig. 1f-g).** In addition, gene expression analysis of autophagy related markers *uvrag,*

111   *vps34, atg14l, FIP200, atg5, atg12, and gabarapl1* did not show any change in *mdx* skeletal

112   muscle as compared to WT **(Fig.S1**). Together, our data suggests that defects in the

113   autophagosome maturation is due to inhibition of vesicle nucleation and elongation of the

114   phagophore in *mdx* skeletal muscle.

115   **Impairment in the SNARE-mediated autophagosomal-lysosomal fusion in *mdx* mice**

116 To clear sequestered cytosolic components the autophagosome must fuse with the lysosome,

117 forming the autolysosome. The process of autophagosome-lysosome fusion is regulated by the

118 SNARE tertiary complex STX17-SNAP29-VAMP8. To achieve autophagosome-lysosome fusion,

119 autophagosome-localized Q-SNARE STX17 must interact with SNAP29 and the lysosomal-

120 localized R-SNARE VAMP8. ATG14L acts as a tethering factor to facilitate the fusion by directly

121 interacting with the STX17-SNAP29 binary complex, and primes it for binding to VAMP8 on

122 lysosomes [38] . We found that STX17 was significantly decreased in *mdx* as compared to WT, while

123 VAMP8 and SNAP29 both showed no change **(Fig.2a-b).** CO-IP with anti-SNAP29 in TA muscle

124 lysates revealed reduced interaction of SNAP29 with STX17 and VAMP8 in *mdx* muscle whereas

125 SNAP29 retained binding with ATG14L **(Fig. 2c)**. CO-IP with an anti-VAMP8 showed less

126 interaction of VAMP8 with STX17, SNAP29, and ATG14L **(Fig. S2a),** confirming reduced

127 autophagosome-lysosome fusion in *mdx* skeletal muscle.

128 Acetylation of STX17 inhibits the interaction between STX17 and SNAP29, and formation of the

129 Q-SNARE complex[39]. Therefore, we asked whether STX17 acetylation is impaired in *mdx* muscle,

130 leading to reduced interaction between the Q-SNARE complexes. We observed decreased

131 acetylation of STX17 in *mdx* muscle compared to WT. We also found increased expression of

132 HDAC2, the primary deacetylase of STX17 [39] in *mdx* muscle **(Fig. S2b-d)**. These data suggest that

133 the reduced interaction in the Q-SNARE complex in *mdx* muscle is not due to increased acetylation

134 of STX17.

135 **Genetic ablation of p47^{phox} promotes autophagosomal maturation without facilitating**

136 **autolysosome formation in *mdx* mice**

137 We have previously shown that genetic deletion of p47^{phox} function in *mdx* mice protects against

138 oxidative stress and improves autophagy (i.e. increased LC3II/I and decreased p62) compared with

6

139   *mdx* [7] . Having established defects at multiple stages in autophagy, including autophagosome

140   maturation and autolysosome formation in *mdx* mice, we asked whether these steps are regulated

141   by Nox2-ROS in *mdx* skeletal muscle. We found increased p-JNK, p-Bcl-2 and JIP-1 protein levels

142   (**Fig. 3b-c**), as well as increased Beclin-ATG14L complex formation and a decrease in the Beclin-

143   Bcl-2 complex (**Fig. 3a**); all consistent with improved vesicle nucleation. We also found an

144   increase in the autophagy elongation complex, ATG5-12 in p47$^{-/-}$/*mdx* mice **(Fig. 3d-e).** We then

145   determined whether autophagosome-lysosome fusion is affected by genetic deletion of p47^{phox} in

146   *mdx* mice. Interestingly, we did not find any improvement in the interaction between STX17-

147   SNAP29-VAMP8 tertiary complexes in p47$^{-/-}$/*mdx* mice as compared to *mdx* mice **(Fig 3f).** In

148   addition, no changes were found in the lysosomal protein LAMP2 and lysosomal hydrolase,

149   Cathepsin B in p47$^{-/-}$/*mdx* mice as compared with *mdx* (**Fig. 3g-h**). Overall, our data indicates that

150   inhibition of Nox2-ROS promotes autophagosome maturation but does not enhance the fusion of

151   autophagosomes with lysosomes in *mdx* mice.

Altered MTs acetylation affects autophagy

153   Emerging evidence shows that reversible acetylation of α-tubulin can regulate MT function, thus,

154   facilitating fusion of autophagosomes to lysosomes[40, 41]. The acetylation status of microtubules is

155   coordinated by deacetylases (HDAC6)[23] and acetyltransferases (MEC-17) [42]. Immunoblot

156   analyses showed that the α-tubulin acetylation levels were significantly decreased in *mdx* muscles

157   as compared to WT (**Fig. 4a-b**). The deacetylase enzyme HDAC6 was increased in *mdx* muscle

158   (**Fig. 4a-b)** whereas the acetyltransferase (MEC17) did not exhibit any change in *mdx* muscle

159   (**Fig.S3a-b).** At the mRNA level, expressions of *hdac6, mec17* genes did not show any change in

160   *mdx* as compared to WT (**Fig.S3c-d**). Autophagosome movement along MT tracks is dependent

161   upon the microtubule motor proteins kinesin and dynein. Kinesin-1 (conventional kinesin or

162 KIF5), is a tetramer of two kinesin heavy chains (KHC, KIF5B) and two kinesin light chains (KLC)

163 [43]. We found that KIF5B was significantly increased in *mdx* muscles whereas KLC and dynein

164 did not change in *mdx* as compared to WT (**Fig.4c-d).** KLCs play a dual role, they direct cargo

165 binding and regulate motor activity. JIP-1 scaffolds with kinesin to link cargo to the kinesin-1

166 complex (KHC/KLC) [44]. These observations raised the question of whether the JIP-Kinesin-1

167 complex is disrupted and thereby decreases binding to MTs and impairing autophagosome

168 transport in *mdx* muscle. Surprisingly, JIP-1 was found to interact with both KLC and JNK in *mdx*

169 mice similar to WT (**Fig.4e**). In addition, we did not find any restoration of acetylated α-tubulin

170 levels in p47$^{-/-}$/*mdx* mice (**Fig. 4f-g).** Overall, our data strongly suggests that microtubule

171 acetylation plays an important role in autophagosome-lysosome fusion in *mdx* mice, which does

172 not appear to be regulated by Nox2-ROS.

173 **HDAC6 inhibition improves MT acetylation and promotes autophagosome-lysosome fusion**

174 **in *mdx* muscle**

175 Acetylated microtubules play an important role in vesicle trafficking and fusion. To assess the

176 relationship of HDAC6 activity with microtubule alterations and impaired autophagic flux,

177 HDAC6 was inhibited with its specific pharmacological inhibitor, Tubastatin A (TubA). TubA

178 was intraperitoneally injected for 2 weeks in 3 week old *mdx* mice, which is just before the onset

179 of disease progression. The dose given to the *mdx* mice was 70mg/kg per day which is equivalent

180 to 8.4mg/kg per day for a human child based on FDA approved mouse to human-equivalence dose

181 calculation guide[45]. TubA restored α-tubulin acetylation levels without altering the protein

182 expression levels of either de-tyrosinated α-tubulin or HDAC6 (**Fig.5a-b)** nor kinesin, JIP-1, or

183 JNK (**Fig.S4a-b**). We next assessed whether the increased acetylation of α-tubulin improved

184 autophagic flux in *mdx* muscle. The autophagosome substrate p62 (SQSTM1) was significantly

8

185 decreased in TubA treated *mdx* muscle while lipidation of microtubule-associated protein 1A/1B-

186 light chain 3 (LC3II), which makes up the autophagosomal membrane showed only a small

187 increase (**Fig. 5c-d**). To further examine the mechanism behind the efficient autophagic clearance

188 in TubA treated *mdx*, we evaluated the autophagosome-lysosome fusion by detecting the binding

189 of SNARE complex proteins. TubA treatment enhanced the interaction of SNAP29 with STX17

190 and VAMP8 **(Fig.5e).** Immunostaining of SNAP29 and VAMP8 showed puncta within the muscle

191 and increased colocalization in TubA treated *mdx* muscle as compared to non-treated, indicative

192 of enhanced autophagosome-lysosome fusion by HDAC6 inhibition **(Fig.5f-g).** In addition, the

193 lysosomal protein LAMP2 and cleaved (active) lysosomal hydrolase cathepsin-B are elevated in

194 TubA treated *mdx* muscle (**Fig. 5h-i**). Overall, our data suggest that the decreased acetylation of

195 α-tubulin in *mdx* muscle inhibits autophagosome-lysosome fusion, which can be recovered upon

196 HDAC6 inhibition.

197 **HDAC6 inhibition recovers acetylation of PrxII and increases total PrxII in *mdx* mice**

198 Prx I and Prx II are specific substrates of HDAC6, their acetylation status provides resistance to

199 hyperoxidation. We have previously shown hyperoxidation and proteolytic degradation of PrxII

200 in *mdx* skeletal muscle [46]. Here, we immunoprecipated PrxII and probed for acetyl lysine and found

201 decreased acetylated PrxII levels in *mdx* mice, which was recovered back to WT in TubA treated

202 *mdx* mice (**Fig 6a**). This was further confirmed by immunoprecipitating acetyl lysine followed by

203 probing for PrxII **(FigS5a).** Total PrxII levels were found to be significantly increased in TubA-

204 *mdx* mice while oxidized PrxII (PrxSO$_{2/3}$) showed no difference as compared to *mdx* (**Fig. 6b-c**).

205 Our findings suggests that TubA did not decrease PrxSO$_{2/3}$ is not surprising, as sulfonation of PrxII

206 is an irreversible oxidative modification [47] . We did find that the ratio of oxidized PrxII to total

207 PrxII is significantly reduced in TubA-treated *mdx* (**Fig. 6b-c**), indicating that the increased

208 acetylation of PrxII prevents its hyperoxidation. To our surprise, we found that stretch activated

209 ROS production was not diminished in diaphragm muscle from TubA treated *mdx* compared to

210 *mdx* (**Fig.6d**). Intriguingly, acetylated PrxII levels were restored back to WT levels in p47$^{-/-}$/*mdx*

211 mice (**Fig. S5b-c**). Total PrxII was increased, PrxSO2/3 decreased, and the ratio of oxidized to

212 total PrxII decreased in p47$^{-/-}$/*mdx* as compared to *mdx*. **(Fig. S5d-e).** These data suggest that either

213 reducing oxidative stress (p47$^{-/-}$/*mdx*) or increasing acetylation of PrxII (TubA) prevents its

214 hyperoxidation and degradation in *mdx* skeletal muscle.

215 **TubA treatment alleviates apoptosis and immune cell infiltration in *mdx* muscle**

216 Impaired autophagy is associated with aggregation of oxidized/misfolded proteins and other

217 cellular constituents, eventually leading to cell death. Immunoblot expression of cleaved/active

218 caspase-3 was found to be significantly reduced in *mdx* mice following treatment with TubA

219 **(Fig.7a-b).** The percentage of TUNEL positive nuclei (*green, marked by white arrows*) were

220 significantly elevated in *mdx* gastrocnemius (GAS) muscle, which were significantly decreased

221 upon treatment with TubA (RI$_{TubA}$ =92.14%, **Fig. 7c-d**). Infiltration of macrophages and other

222 immune cells is an important and pathogenic feature of dystrophin-deficient muscle, even at

223 asymptomatic stage of disease progression. We have stained GAS muscle cross-sections with anti-

224 CD68 antibody to identify CD68+ macrophages. We found a significant decrease in CD68^{+}

225 immune cells *(green, marked by white arrows)* in TubA treated *mdx* skeletal muscle (RI

226 $_{TubA}$=63.10%, **Fig. 7e-f**), indicating decreased infiltration of macrophages in the endomysium of

227 skeletal muscles.

228 **Amelioration of dystropathology and improvement in muscle functional assessment**

229 **following TubA treatment**

230   Since pharmacological inhibition of HDAC6 improved MT acetylation, restored autophagic flux

231   by promoting autophagosome-lysosome fusion, and decreased inflammation and apoptosis we

232   next investigated whether TubA reduced muscle damage and improved muscle performance.

233   Treatment of *mdx* mice with TubA prevented the increase in serum creatine phosphokinase (CPK

234   activity (RI_{TubA}=133.81%, **Fig. 8a**), a widely used clinical marker of muscle damage. The etiology

235   of DMD can be explained by loss of membrane integrity due to dystrophin deficiency which results

236   in degeneration of myofibers. To determine whether TubA affects sarcolemmal integrity, we

237   intraperitoneally injected mice with Evans blue dye (EBD), which penetrates non-specifically into

238   any cell with disrupted/leaky membranes. At 24 h after injection, EBD accumulated abundantly in

239   *mdx* muscles as compared to WT muscles **(Fig. 8b),** confirming membrane permeability due to the

240   loss of dystrophin. Notable, TubA treatment significantly blunted EBD uptake into the DIA muscle

241   of *mdx* mice. This observation was further confirmed by fluorescence staining of cross-sections of

242   DIA muscles, the number of EBD positive fibers were reduced in *mdx* mice treated with TubA (RI

243    $_{TubA}$=85.81%, **Fig.8c**).

244   We next assessed the histopathological features of TA muscles from WT, *mdx* and TubA treated

245   *mdx* mice by H& E staining. We observed severe necrosis (*marked by black arrow*), regenerating

246   fibers with central nuclei *(marked by black arrow head)*, and fat deposition in the interstitial space

247   *(marked by black asterisk)* of dystrophic muscle as compared to WT muscles. Notably, overall

248   necrotic myofibers, central nuclei, and fat depositions were reduced in TubA treated *mdx* **(Fig.8d).**

249   We further quantified histological sections of TA muscles by immunostaining with α-laminin

250   (*green*) and DAPI (*blue)* to analyze the cross-sectional area (CSA) and centronucleated myofibers

251   in treated and untreated *mdx* mice **(Fig.8d)**. A drastic increase in the percentage of fibers with

252   centralized nuclei was observed in *mdx* TA muscle as compared to WT (46% versus 1.2%), which

11

253 was significantly reduced in TubA-treated *mdx* muscle (RI$_{TubA}$= 52.2%, **Fig. 8e**). TA muscle from

254 *mdx* mice showed decreased cross-sectional area (CSA) as compared to WT, which was partially

255 prevented with TubA treatment as exhibited by the distribution of Minimal Feret's diameter (**Fig**

256 **8f).** DMD patients suffer from progressive muscle weakness, eventually leading to immobility and

257 respiratory failure. To examine whether TubA improves muscle function and strength, *in-vivo*

258 muscle functional performance was assessed by grip strength. Grip strength was conducted after

259 completion of 2weeks of TubA treatment in *mdx* mice. Skeletal muscle strength was significantly

260 improved in TubA treated *mdx* mice as compared to non-treated *mdx* mice (RI$_{TubA}$=113.29%, **Fig.**

261 **8g-h).** Finally, to determine the effects on contractile function, we compared the force-generating

262 capacities of untreated and TubA-treated *mdx* diaphragm muscle strips electrically stimulated *ex*

263 *vivo.* TubA-treated *mdx* mice demonstrated significantly greater diaphragmatic force production

264 over a broad range of stimulation frequencies (0 to 200 Hz) (**Fig. 8i, Table 1).** In addition, TubA

265 treated *mdx* EDL muscle was significantly protected from eccentric contraction induced force loss

266 compared to *mdx* muscle (**Fig. 8j, Table 1).**

267 **Discussion**

268 Previous studies have shown that defective autophagy and disorganized MT network play an

269 important role in disease progression and contributes to DMD pathogenesis before the

270 manifestation of severe phenotypes [11,48, 49, 50, 51.] Therefore, reverting autophagic dysfunction could

271 be an efficient approach to slow the onset of disease progression and improve the muscle function

272 in DMD patients. Our group was the first to identify that Nox2 mediates MT alterations and

273 autophagic dysfunction in dystrophic muscle [7, 14]. MTs regulate autophagy through their

274 scaffolding and transport functions. Acetylated MTs induce autophagy by facilitating intracellular

275 trafficking and fusion of autophagosomes with lysosomes[18, 19, 52]. Despite the number of

12

276   investigations, no consensus about the role of tubulin post translational modifications in regulating

277   autophagic flux in DMD have been reached. We are the first to report that autophagy is

278   differentially controlled by redox and acetylation modifications in *mdx* mice (**Fig. 9**). We provide

279   evidence that genetic ablation of Nox-2 in *mdx* mice promotes autophagosome maturation without

280   facilitating autophagosome-lysosome fusion. Further, our study reveals alterations in MT

281   acetylation in dystrophin-deficient muscle, which is not restored back in Nox-2 ablated *mdx* mice.

282   Pharmacologically targeting HDAC6 restored MT acetylation, rescued autophagy by accelerating

283   fusion and content degradation, restricted muscle damage and improved muscle function in *mdx*

284   mice.

285   Autophagosome biogenesis/maturation includes phagophore nucleation, expansion, and closure of

286   phagophore membranes, generating the complete autophagosome[36]. Initiation of autophagy

287   requires the PI3KClassIII complex consisting of VPS34, VPS15, Beclin1/BECN1 and ATG14L.

288   Emerging evidence suggests impaired autolysosome clearance in VPS15 deficient muscle and the

289   muscle phenotype evocative of lysosomal myopathies [53]. A study by Nascimbeni et al., have shown

290   that alterations in VPS15, VPS34 and BECN1 lead to impaired endosome and lysosomal

291   maturation in Danon Disease and Glycogen Storage Disease (GSDII) [54]. In the current study, we

292   found that the PI3KclassIII complex was disrupted in *mdx* muscle, with a significant decrease in

293   ATG14L and VPS34, whereas VPS15 was found to be increased. Intriguingly, we also found

294   reduced interaction of Beclin-ATG14L complex whereas Beclin-Bcl-2 complex formation, which

295   is known to inhibit autophagic induction, is increased in *mdx* muscle. This indicates disruption in

296   the formation of vesicle nucleation. During starvation, tubulin acetylation signals kinesin

297   recruitment to the MTs, with subsequent JNK activation and phosphorylation of Bcl-2, which

298   allows the release of Beclin from Beclin–Bcl-2 complexes to initiate autophagosome formation.

13

299   [55]. We found decreased JNK activation, likely due to reduced levels of the scaffolding protein JIP-

300   1, in *mdx* muscles and reduced phosphorylation of Bcl-2 (S70), thus inhibiting Beclin-ATG14L

301   association for vesicle nucleation. In addition, WIPI-1, which recruits lipid phosphatidylinositol-

302   3 phosphate (PI3P) and mediates recruitment of the ATG5-12/16L1 complex and the LC3

303   lipidation, was found to be reduced in skeletal muscle from *mdx* mice. Taken together, our data

304   suggest that defects in autophagosome maturation is mediated by inhibition of the Kinesin-JIP-

305   JNK pathway in dystrophic mice.

306   SNARE associated proteins play a major role in membrane-mediated events of autophagosome-

307   lysosome fusion, another crucial step in autophagy process. Recent studies have highlighted the

308   role of STX17-SNAP29-VAMP8 Q-SNARE tertiary complex in promoting autophagosome-

309   lysosome fusion. [19, 56] We revealed that the blockage of autophagosome-lysosome fusion in *mdx*

310   mice was not due to altered expressions of SNARE associated proteins but due to the inhibition of

311   the interaction of STX17 and VAMP8 with SNAP29, which culminates in accumulation of

312   autophagosomes [7]

313   Previous work from our lab has shown that genetic ablation of Nox2-ROS improved autophagy in

314   *mdx* mice. Nevertheless, the detailed mechanisms by which autophagy was rescued in the $p47^{-/-}$

315   /*mdx* mouse was not evaluated, which is required to improve the therapeutic outcomes for DMD

316   patients. Our current data showed that $p47^{-/-}$/ *mdx* mice prevented the defects of autophagosome

317   maturation by promoting vesicle nucleation and elongation of autophagosomes. However, our data

318   revealed that genetic inhibition of Nox-2 was not able to promote the interaction between STX17-

319   SNAP29 and VAMP8-SNAP29 and thus cannot promote autophagosome-lysosome fusion and

320   content degradation in *mdx* mice. These finding may explain why we only observed partial rescue

321   of dystrophic pathology in the $p47^{-/-}$/*mdx* mouse[7] .

14

322   Based on the above findings, we speculate that autolysosome formation in *mdx* muscle is redox

323   independent, leading us to explore the mechanisms that underlie the failure of delivery of

324   autophagosomes and its fusion with lysosomes. Protein acetylation controls autolysosome

325   formation and improves autophagic flux[19, 39, 57]. Emerging evidences suggests that HDAC2

326   promotes autophagy by causing deacetylation of STX17, which increases its binding with SNAP29

327   and promotes the Q-SNARE complex formation [39]. Interestingly, our findings revealed the

328   deacetylation of STX17 and increased HDAC2 in *mdx* mice, which suggests that reduced

329   interaction of STX17-SNAP29-VAMP complex is independent of the STX17 acetylation and

330   HDAC2.

331   Previous studies from our lab and others have reported dystrophin deficiency results in

332   disorganized MT lattice network and elevated MT tubulin modifications (detyrosinated α-tubulin)

333   in *mdx* muscle [14,58] . Post translational modifications of MTs, in particular acetylation, have been

334   shown to facilitate autophagosome formation and serve to direct mature autophagosomes for

335   fusion and degradation[41, 59, 60]. In the present study, we find decreased acetylated α- tubulin in *mdx*

336   mice, with increased protein expressions of the deacetylase enzyme, HDAC6. Accumulating

337   evidence suggests that JIP-1 mediates and regulates the binding of cargo to the Kinesin-1 complex

338   via KLC on the microtubule track. Activated JNK regulates the binding of cargo to KLC by

339   mediating the release of cargo once they have reached the lysosomes for fusion. Ittner et al. have

340   shown that impaired binding of JIP-1 to the kinesin-1 complex disrupted the anterograde axonal

341   transport of cargo along MTs in Alzheimer's disease[61]. Surprisingly, in dystrophic muscle, JIP-1

342   interacts with KLC and JNK, forming a KLC-JIP-JNK complex. We therefore speculate that

343   decreased MT acetylation in *mdx* muscle can prevent the binding of KLC-JIP-JNK on the MT

344   track, leading to inhibition of autophagosome transport and its fusion with lysosomes.

15

345   HDAC6 inhibition exerted beneficial effects by improving autophagic dysfunction through MT

346   acetylation in several pathophysiological conditions such as, Huntington's disease (HD)[27]spinal

347   cord injury [19], osteoarthritis [33], and doxorubicin-induced cardiomyopathy[30]. HDAC6 has unique

348   structure and properties, exerting both enzymatic and non-enzymatic effects on cellular functions.

349   In addition to two catalytic domains which deacetylates cytoplasmic non-histone proteins, it also

350   possesses a non-enzymatic zinc-finger ubiquitin-binding domain (UBD) at its C-terminus[62].

351   Through its UBD, HDAC6 interacts with ubiquitinated protein aggregates to promote loading and

352   transport along the microtubules for proper degradation. Given this dual role of HDAC6 in

353   regulating the response to cellular stress, pharmacological inhibition of its enzymatic activity, as

354   opposed to knock-down of protein content, has been shown to be a novel and promising therapeutic

355   strategy for several diseases[63]. We selected TubA, which stands out as a potent and highly specific

356   HDAC6 inhibitor with an IC_{50} of 15 nM and has a strict selectivity for HDAC6 over all other

357   HDACs (over 1000-fold) except for HDAC8 (57 folds) [64]. Unlike other HDAC inhibitors, TubA

358   exhibits no toxicities such as fatigue, nausea, or thrombocytopenia, thus making HDAC6 a most

359   suitable and promising therapeutic target [64]. We assessed TubA dosing in *mdx* cohorts at 30mg/kg

360   every other day for 4weeks and did not observe any muscle functional recovery, although serum

361   CPK levels were reduced. **(Fig.S6a-b)**.We further assessed TubA dosing in *mdx* cohorts at

362   70mg/kg every day for 2 weeks. Interestingly, TubA treatment at this dose showed improvement

363   in muscle contractile properties and strength, and reduced serum CPK levels in *mdx mice*. Our data

364   shows that HDAC6 inhibition specifically promoted tubulin acetylation without affecting DT-

365   tubulin levels in *mdx* mice. However, HDAC6 inhibition was not able to activate JIP/JNK

366   signaling as assessed by phospho-JNK and thus, autophagosome maturation was not improved in

367   TubA treated *mdx*. HDAC6 inhibition was recently reported to restore neuronal autophagy flux by

16

368   increased LC3II and decreased p62 aggregates in neurodegenerative disorders[27, 65]. TubA

369   treatment promoted the autophagosome-lysosome fusion by SNARE machinery in SCI[19].

370   Consistent with these findings, we found increased LC3II and reduced p62 aggregates, which

371   indicates efficient autophagic clearance in TubA treated *mdx*. TubA treated *mdx* mice showed

372   increased interaction of STX17 and VAMP8 with SNAP29, thus facilitating the fusion and

373   formation of autolysosomes, as well as enhanced lysosomal function. Altogether, our data support

374   a role for HDAC6 regulating autophagic flux by decreasing MT acetylation and inhibiting protein

375   aggregate trafficking and fusion of autophagosome-lysosome in skeletal muscle from *mdx* mice,

376   which is reversed upon HDAC6 inhibition with TubA.

377   HDAC6 may have a role in regulating redox balance within the cell, as HDAC6 has been shown

378   to deacetylate redox regulatory proteins, PrxI and PrxII[25]; and once deacetylated PrxI and PrxII

379   lose their antioxidant capacity. HDAC6 inhibition recovered acetylation of Prx and provided

380   protection against oxidative stress in Aβ-induced Alzheimer's disease (AD) [24], 6-OHDA induced

381   Parkinson's disease (PD) model [29], and myocardial ischemia/reperfusion (MI/R) [32], suggesting a

382   new mechanism regulating redox balance. In the current study, our results showed that acetylation

383   levels of PrxII were decreased in *mdx* muscle, and TubA treatment recovered both acetylation

384   levels of PrxII and total PrxII in *mdx* mice. Our previous findings show that PrxII overexpression

385   protects *mdx* mice from eccentric contraction induced force loss[46]. However, we did not observe

386   any change in either oxidized PrxII (PrxSO2/3) or stretch dependent ROS production in *mdx* mice

387   treated with TubA. Intriguingly, p47^{-/-}/*mdx* mice showed reduced levels of oxidized PrxII

388   (PrxSO2/3), increased PrxII acetylation, but did not increase MT acetylation. Thus, there appears

389   to be cross-talk between HDAC6 and Nox2 in dystrophic skeletal muscle that we have yet to

17

390   understand, and doing so will be essential for developing effective therapeutics for maintaining

391   muscle homeostasis in DMD patients.

392   Our data reveals that TubA has the potential to act on the downstream pathogenic events of

393   dystropathology. TubA treatment attenuated apoptosis, decreased levels of CD68+ macrophages

394   infiltrated into the muscle, maintained sarcolemmal integrity, and remarkably reduced serum CK

395   levels in *mdx* mice. Quantitative analysis of Hematoxylin/eosin staining showed significant

396   reduction in the centralized nuclei and increased CSA in TA *mdx* muscle following treatment with

397   TubA. In DMD patients, even at very young ages, weakness in hand strength is observed as a

398   generalized effect of dystrophin deficiency. Loss of grip strength was observed in *mdx* mice while

399   TubA treated *mdx* mice showed significant improvement in muscle strength. Diaphragm is the

400   most severely affected skeletal muscle in dystrophic mice, and diaphragm dysfunction is a major

401   cause of respiratory failure in DMD patients. TubA-treated *mdx* mice showed significantly greater

402   diaphragm force production and decreased ECC induced force loss. These finding indicate that

403   HDAC6 inhibition not only restores autophagy flux by regulating MT acetylation but it extended

404   its efficacy to alleviate many symptoms due to loss of dystrophin in DMD

405   In conclusion, our study suggests that defects in autophagy are regulated by both redox and

406   acetylation modifications in *mdx* mice. Evidence provided in this study confirms the role of

407   HDAC6 in deacetylating MTs, which led to the disruption of autophagosome-lysosome fusion in

408   dystrophin deficient mice. HDAC6 inhibition holds the potential to counteract the alteration of the

409   MTs and restore impaired autophagic flux in dystrophic skeletal muscle **(Fig.9).** This pre-clinical

410   study suggests that targeting specific histone deacetylase, HDAC6 served as an effective tool in

411   preventing disease progression and improving muscle strength and function **(Table 1)**, supporting

412   the translational potential of TubA into clinical research for DMD patients. In view of our data,

18

413   combinatorial therapeutic approaches are currently underway in our laboratory to assess the

414   efficacy of TubA and Nox-2 pharmacological inhibitor in ameliorating pathological changes in

415   DMD.

416

Material and Methods

Antibodies and Reagents

Tubastatin A and PEG300 were purchased from Selleck Chem, DCFH-DA (6-carboxy-2′,7′-dichlorodihydrofluorescein diacetate) was from Invitrogen. DMSO and Evans Blue Dye were purchased from Sigma Aldrich. Tween-80 from Fischer Scientific. Protein A Magnetic Beads , Mini-Protean TGX stain free gels, and Immun-Blot® PVDF Membrane, Clarity western ECL substrate were purchased from Bio-Rad. Anti-beclin, anti-p-bcl-2, anti-vps34, anti-vps15, anti-JNK, anti-p-JNK, anti-atg5-12, anti-atg7, anti-atg4b, anti-α-tubulin, anti-HDAC6, anti-p62, anti-caspase-3, and anti-LC3 antibodies were from Cell Signaling Technology. Anti-GAPDH (glyceraldehyde-3-phosphate dehydrogenase) and anti-dynein were purchased from EMD Millipore. Anti-CD68, anti-LAMP2, anti-Cathepsin-B, anti-SNAP29 were purchased from Santa Cruz Biotechnologies. Anti-WIPI1, anti-snap29, anti-stx17, anti-vamp8, anti-KIF5B, anti-KLC, anti-detyrosinated, anti-Prx-SO3, and anti-α-laminin were from Abcam. Anti-acetylated tubulin, anti-bcl-2, anti-atg14, anti-MAPKK, anti-JIP-1, anti-prxII were from Millipore Sigma. Secondary antibodies for immunofluorescence (Alexa Fluor® 594 donkey anti-rabbit, Alexa Fluor® 488-donkey anti-rabbit, Alexa Fluor®594-goat anti-mouse), and ProLong™ Gold Antifade Mountant with DAPI were purchased from Invitrogen. Microscopic slides was purchased from Denville Scientific Inc. Detailed information about antibodies and dilution can be found in **Supplementary Table 1 and 2.**

Mice

C57BL/10ScSnJ (WT) and C57Bl/10ScSn-Dmd*mdx*/J (*mdx*) were purchased from Jackson Laboratories (Bar Harbor, ME) and bred following their breeding strategy. Mice with a genetic deletion of the Nox-2 scaffolding subunit p47^{phox} (p47$^{-/-}$) were obtained from The Jackson Laboratory (B6 (Cg)-Ncf1m1J/J) and bred onto the *mdx* background as previously described [7]. All animals used for experiments were males between 3-6 weeks of age. All animal studies were conducted in accordance with ARRIVE (Animal Research: Reporting of In Vivo Experiments). Mice were housed in a specific pathogen free (SPF) facility on a 12hr light/dark cycle. All mice were monitored daily and drug tolerability evaluated on the basis of body weight and clinical signs. After treatment period, mice were sacrificed by deep anesthesia followed by cervical dislocation as approved by the Institutional Animal Care and Use Committee (IACUC) of Baylor College of Medicine. Skeletal muscles were quickly excised, and either placed in Krebs-Ringer buffer for tissue experiments, snap frozen in liquid nitrogen for biochemical and molecular experiments, or in 10% formalin for histological experiments. We employed basic methods to analyze the preclinical experiments (TREAT-NMD) [66]

HDAC6 Inhibitor treatment

452 For pharmacological inhibition of HDAC6, HDAC6-Specific inhibitor TubastatinA (TubA)
453 (Selleck-Chem, USA) was dissolved in 4% dimethyl sulfoxide (DMSO), 30% PEG300 and 66%
454 MilliQ with a final concentration of 2.5 mg/mL, and was freshly prepared each day. TubA was
455 intraperitoneally *(i.p.)* injected into 3 week-old *mdx* mice (onset of disease progression) at the
456 dosage of 70 mg/kg b.w. once a day for 2 weeks.

457 **Fore-limb Grip strength analysis**

458 Fore-limb grip strength was performed to assess the effects of TubA on recovery of muscle
459 strength of *mdx* mice. The grip strength meter (Columbus Instruments, OH) was positioned
460 horizontally and mice were held by the tail. Mice were allowed to grasp the smooth metal rod with
461 their forelimbs only and then were pulled backward by the tail. The force applied to the metal rod
462 at the moment the grasp was released and recorded as the peak tension. The test was repeated 5
463 consecutive times within the same session and the average value from the 5 trials was recorded as
464 the grip strength for that animal. In order to avoid modifications induced by the body weight of
465 the mice in the latency of staying on the grip strength meter, the data have been normalized with
466 body weight of mice. The grip strength test was conducted by the same investigator in order to
467 avoid variability in performing experiment, and the investigator was blinded to the treatment
468 group.

469 **Serum Collection**

470 Blood was collected from the hepatic portal vein of mice immediately following sacrifice and left
471 at room temperature for 30 min to achieve coagulation. Serum was then separated from other blood
472 fractions by centrifugation at 1,000 g for 10 min and stored at −80 ºC for further use. CK activity
473 in the serum was measured using Creatine Kinase Activity Assay Kit (My BioSource) following
474 the manufacturer's instruction.

475 **Ex-Vivo EDL Eccentric force measurements**

476 Muscle contractile force measurement was conducted by using an *ex-vivo* muscle test system. In
477 brief, the mice were anesthetized with isoflurane, the hind limb was excised and immediately
478 placed in a bicarbonate-buffered solution (120 mM NaCl, 4 mM KCl, 1 mM $MgSO_4$, 1 mM
479 NaH_2PO_4, 25 mM $NaHCO_3$, and 2 mM $CaCl_2$, 10mM glucose) equilibrated with 95% O_2-5% CO_2
480 (pH7.4) for dissection. The proximal and distal tendons were tied with braided silk suture thread
481 (4-0, Fine Science Tools) and mounted in a muscle bath containing bicarbonate-buffered solution
482 continuously bubble with 95%O_2, 5% CO_2 between a fixed hook and a dual-mode lever system
483 (305C-LR-FP, Aurora Scientific Inc., Aurora, ON, Canada) and allowed to equilibrate to 30ºC for
484 10 minutes. The stimulation protocol consisted of supramaximal electrical current delivered
485 through platinum electrodes using a biphasic high-power stimulator (701C; Aurora Scientific).
486 Optimum length (Lo) was determined with a series of twitch stimulations measured using a hand-

487 held electronic caliper, after which the muscle underwent 10 eccentric contraction with 3 minutes
488 rest between each contraction so as to not elicit muscle fatigue. Each eccentric contraction
489 consisted of a 200 ms isometric tetanus (150Hz) followed by stretch from 100% to 110% of Lo at
490 0.5Lo/s and then shortened to Lo passively. Following the 10 eccentric contractions the muscle
491 was removed from the organ bath, trimmed of connective tissue, blotted dry, and weighed. Data
492 were analyzed using the dynamic muscle control and analysis software (Aurora Scientific Inc.).

493 **Ex-Vivo Diaphragm Isometric force measurements**

494 Diaphragm (DIA) muscle was dissected from mice and one end tied to a fixed hook and the other
495 to a force transducer (F30, Harvard Apparatus) using silk suture (4-0) in bicarbonate-buffered
496 solution continuously gassed with 95% O_2–5% CO_2 at 30ºC. Contractile properties were assessed
497 by passing a current between two platinum electrodes at supramaximal voltage (PanLab LE 12406,
498 Harvard Apparatus) with pulse and train durations of 0.5 and 250 ms, respectively. Muscle length
499 was adjusted to elicit maximum twitch force (optimal length, Lo) and the muscle was allowed a
500 10-min equilibration period. To define the force-frequency characteristics, force was measured at
501 stimulation frequencies of 1, 5, 10, 20, 40, 60, 80, 120, 150 and 200 Hz every 1 min. At the end of
502 the contractile protocol, muscle length was measured using a hand-held electronic caliper, fiber
503 bundles removed from the organ bath and trimmed of excess bone and connective tissue, blotted
504 dry and weighed. Muscle weight and Lo were used to calculate normalized forces expressed as
505 N/cm^2

506 **ROS measurements**

507 Diaphragm intracellular ROS was measured using 6-carboxy-20,70-dichlorodihydrofluorescein
508 diacetate (DCFH-DA) (Invitrogen, Carlsbad, CA) as previously described[14] Briefly, diaphragm
509 muscle optimal length was determined as described above followed by incubation with DCFH-
510 DA for 30 min, washed using the physiological saline solution and de-esterified for an additional
511 30 min at 25˚C. All cell-loading and imaging was performed in the dark to prevent light induced
512 oxidation of DCFH-DA. DCF was excited at 470/20 nm using a Sutter Lamda DG-5 Ultra-high-
513 speed wavelength switcher and emission intensity was collected at 535/48 nm on a charge coupled
514 device (CCD) Camera (CoolSNAP MYO, Photometrics, Tucson, AZ) attached to an Axio
515 Observer (Zeiss) inverted microscope (20X objective, 0.5 NA) at a rate of 0.2 Hz. Alterations in
516 the rate of ROS production were baseline corrected and calculated over the final minute of the
517 stretch period.

518 **Western blotting and Immunoprecipitation**

519 TA muscle from hind limb of the mice were isolated and lysed with ice-cold RIPA buffer
520 containing protease and phosphatase inhibitors, and centrifuged at 13,500rpm for 10 min. The
521 supernatant was retained, aliquoted, and the protein content was quantified using the bicinchoninic

522 acid (BCA) Assay Kit. A volume corresponding to 10 μg of protein was diluted with a Laemmli
523 sample buffer (BioRad), and heated at 100 °C for 5 min. Protein samples were separated via 4-
524 15% and 4-20% SDS-PAGE and then transferred to polyvinylidene difluoride (PVDF)
525 membranes, which were blocked with 5% non-fat milk or 5% BSA (dissolved in Tris-buffered
526 saline, pH 7.4, and 0.2% Tween 20, TBST) for 60 min at room temperature.

527 For immunoprecipitation, total protein lysates were prepared and quantified as described above.
528 Protein lysates (1000μg) were incubated with protein A magnetic beads (BioRad) as per the
529 manufacturer's instructions. Protein complexes were analyzed by western blotting using indicated
530 antibodies (Beclin-1, ATG14L, Bcl-2, JIP-1, JNK, KIF5B, KLC, SNAP29, VAMP8, STX17,
531 Prx2, acetyl lysine). Immunoblots were incubated overnight at 4 °C with primary antibodies. The
532 following day, membranes were washed and incubated with secondary antibodies for 60min at
533 room temperature. Clarity western ECL substrate (Bio-Rad) was added on the membrane and the
534 signals were visualized by ChemiDoc Imaging system (Bio-Rad). The bands were quantified using
535 densitometric analysis by the ImageLab Software.

Histology and Immunofluorescence

537 The skeletal muscles (TA and GAS) were carefully excised from hind limb of mice and post-fixed
538 in 10%formalin overnight. Paraffin blocks were then prepared after dehydration, clearing, and wax
539 impregnation. Transverse Sections (T.S.) of 4μm thickness were cut with a rotary microtome,
540 deparaffinized in xylene and gradient of alcohol were subjected to histological or
541 immunofluorescence staining.

542 For H&E staining, the slides were stained in hematoxylin solution for 20–30 min and rinsed in
543 running water three times. Slides were then stained in eosin solution for 1–2 min, dehydrated in
544 graded ethanol and xylene, and covered using DPX paramount for further imaging. For
545 immunofluorescence, serial muscle cross-section (4μm) were cut from each paraffin block by
546 rotatory microtome. The sections were placed on coated slides (Denville Scientific Inc.) and dried
547 at 60 °C in a hot air oven. Sections were deparaffinized, rehydrated, and underwent an antigen
548 retrieval method using citrate-EDTA solution incubated at 96 °C for 20 min in water bath. After
549 dipping the slide in distilled water, the sections were blocked with 3% BSA for 60min at room
550 temperature, and incubated with the primary antibodies overnight at 4°C followed by secondary
551 antibodies at room temperature for 1 h. Primary antibodies include SNAP29, VAMP8, CD68, and
552 α-laminin. Secondary antibodies include Alexa Fluor 488 and 594. Tissue sections were mounted
553 with Prolonged Gold Antifade with DAPI (Invitrogen). All images were taken with Fluorescent
554 microscope (ECHO, CA) and analysis was carried out by ImageJ software.

555 For CD68 quantification, images acquired from five different optical fields of GAS muscle cross-
556 section (40X magnification) and the number of CD68+ immune cells were counted per area (μm^2).

557 The CSA and centralized nuclei were measured based on α-laminin staining and DAPI stained
558 nuclei respectively. CSA was quantified by minimum Feret's diameter and central nucleation was
559 quantified as % fibers with central nuclei. TA muscle cross-sections were used for quantification.
560 All the immunofluorescence images were quantified using Image J software (NIH, USA).

561 **Colocalization analysis**

562 For double immunofluorescence, two primary antibodies (SNAP29 and VAMP8) were incubated
563 on the same gastrocnemius (GAS) tissue sections. To quantify the degree of colocalization
564 between the anti- SNAP29 and anti-VAMP8 staining, Pearson's correlation coefficient was
565 performed using ImageJ Software.

566 **RNA extraction and Gene expression analysis**

567 Total RNAs were extracted from gastrocnemius (GAS) muscles using TRIzol reagent (Invitrogen)
568 according to the manufacturer's protocol. Gene expression was verified by using cDNA synthesis
569 kit (Company name) for reverse transcription and Real Mastermix for PCR following
570 manufacturer's instructions. The primers used were as follows:

571 BECN1-FWD (5' AGG CTG AGG CGG AGA GAT T-3'),

572 BECN1-REV (5'- TCC ACA CTC TTG AGT TCG TCA T-3');

573 ATG5-FWD (5'-ATCAGACCACGACGGAGCGG-3'),

574 ATG5-REV (5'-GGCGACTGCGGAAGGACAGA-3');

575 ATG12-FWD (5'- ACAAAGAAATGGGCTGTGGAGC-3'),

576 ATG12-REV (5'- GCAGTAATGCAGGACCAGTTTACC-3');

577 ATG14L-FWD (5'- GCAGCTCGTCAACATTGTGT-3'),

578 ATG14L-REV (5'-TGCGTTCAGTTTCCTCACTG-3');

579 VPS34-FWD(5'-TGTCAGATGAGGAGGCTGTG-3'),

580 VPS34-REV(5'-CCAGGCACGACGTAACTTCT-3');

581 GABARAPL1-FWD (5'- CGGTCATCGTGGAGAAGGCT-3'),

582 GABARAPL1-REV (5'- CCAGAACAGTATAACGGCAACTCC-3');

583 FIP200-FWD(5'-ACCGTGCACCTGCTATTCCT-3'),

584   FIP200-REV (5' CATCATGGACAAGCCCTTCA-3');

585   UVRAG-FWD (5' CAA GCT GAC AGA AAA GGA GCG AG-3'),

586   UVRAG-REV (5'- GGA AGA GTT TGC CTC AAG TCT GG-3');

587   HDAC6-FWD(5'-AAGTGGAAGAAGCCGTGCTA-3'),

588   HDAC6-REV (5'- CTCCAGGTGACACATGATGC -3')';

589   MEC17/ATAT1-FWD (5'- ACTGA AGGAC ACCTC AGCCC GA -3'),

590   MEC17/ATAT1-REV(5'- TACCT CATTG TGAGC CTCCC GG-3')

591   **Evan's Blue Dye uptake**

592   To assess the membrane integrity of WT, *mdx*, and TubA treated *mdx* mice, Evans Blue Dye (EBD)
593   was injected to the animal as described by Millay et al [67]. EBD (10mg/ml) was dissolved in PBS
594   (pH 7.4) and sterilized by passage through membrane filters with a 0.2-mm pore size. Mice were
595   injected intraperitoneal *(i.p.),* with 0.1 ml/10g body weight with EBD 24h prior to the completion
596   of two week treatment with TubA. After 24h, DIA muscles were harvested from all the mice
597   groups and sectioned using rotatory microtome. EBD positive fibers showed a bright red emission
598   under fluorescent microscope. All sections were examined, photographed and muscle fiber
599   counted under a fluorescence microscope (ECHO, CA).

600   **TUNEL ASSAY**

601   GAS isolated from hind limb of mice fixed in 4% formalin overnight and then paraffin-embedded
602   muscles sections (4μm) were assessed by terminal deoxynucleotidyltransferase-mediated dUTP
603   nick end labeling (TUNEL) assay with an in situ Cell Death Detection Kit (Biovision Inc., CA,
604   USA) as per the manufacturer's instructions. Antigen retrieval was performed and slides were then
605   blocked in 3% bovine serum albumin for 1hr at RT and incubated in anti-α-laminin overnight at
606   4ºC. The following day, slides were incubated in donkey anti-rabbit AF594 and then stained with
607   Prolong gold antifade reagent with DAPI (Invitrogen).Tissue sections were examined under
608   fluorescence microscope (ECHO, CA). TUNEL positive nuclei were counted manually as a co-
609   localization of TUNEL + nuclei with DAPI and expressed as a percentage of the TUNEL + nuclei
610   per total number of DAPI stained nuclei obtained from five different optical field per muscle
611   section (40X Magnification). Total number of DAPI stained nuclei were counted using Image J
612   software (NIH).

613   **Statistical analysis**

614

615   Statistical analysis were performed using Origin Pro Software (OriginLab Corporation,

616   Northhampton, MA, USA). Differences between two groups were analyzed using Student's *t*-tests

617   and normality tests. Differences between means of multiple groups were analyzed by one or two-

618   way analysis of variance *ANOVA* followed with Tukey *post-hoc* tests. Values of *p*<0.05 (95%

619   confidence) were considered statistically significant. Data are represented by box plots with mean

620   (empty checker box within the box), median (solid bar), SD (whisker), SE (box). The number of

621   mice used in groups for each parameter are indicated in figure legends. Recovery index (RI_{TubA})

622   was calculated as $((mdx+TubA)-(mdx))/((WT)-(mdx)) \times 100$ [66].

623

References

1. Himic, V. & Davies, K.E. Evaluating the potential of novel genetic approaches for the treatment of Duchenne muscular dystrophy. *Eur J Hum Genet* (2021).

2. Duan, D., Goemans, N., Takeda, S., Mercuri, E. & Aartsma-Rus, A. Duchenne muscular dystrophy. *Nat Rev Dis Primers* **7**, 13 (2021).

3. Min, Y.-L. *et al.* CRISPR-Cas9 corrects Duchenne muscular dystrophy exon 44 deletion mutations in mice and human cells. *Science Advances* **5**, eaav4324 (2019).

4. Porter, G.A., Dmytrenko, G.M., Winkelmann, J.C. & Bloch, R.J. Dystrophin colocalizes with beta-spectrin in distinct subsarcolemmal domains in mammalian skeletal muscle. *The Journal of cell biology* **117**, 997-1005 (1992).

5. Spinazzola, J.M. & Kunkel, L.M. Pharmacological therapeutics targeting the secondary defects and downstream pathology of Duchenne muscular dystrophy. *Expert Opin Orphan Drugs* **4**, 1179-1194 (2016).

6. Khairallah, R.J. *et al.* Microtubules underlie dysfunction in duchenne muscular dystrophy. *Science signaling* **5**, ra56 (2012).

7. Pal, R. *et al.* Src-dependent impairment of autophagy by oxidative stress in a mouse model of Duchenne muscular dystrophy. *Nature Communications* **5**, 4425 (2014).

8. Boya, P., Reggiori, F. & Codogno, P. Emerging regulation and functions of autophagy. *Nature Cell Biology* **15**, 713-720 (2013).

9. De Palma, C. *et al.* Autophagy as a new therapeutic target in Duchenne muscular dystrophy. *Cell Death Dis* **3**, e418 (2012).

10. Whitehead, N.P. *et al.* Validation of ultrasonography for non-invasive assessment of diaphragm function in muscular dystrophy. *The Journal of physiology* **594**, 7215-7227 (2016).

11. Prins, K.W. *et al.* Dystrophin is a microtubule-associated protein. *The Journal of cell biology* **186**, 363-369 (2009).

12. Belanto, J.J. *et al.* Microtubule binding distinguishes dystrophin from utrophin. *Proceedings of the National Academy of Sciences* **111**, 5723-5728 (2014).

13. Percival, J.M. *et al.* rAAV6-microdystrophin rescues aberrant Golgi complex organization in mdx skeletal muscles. *Traffic (Copenhagen, Denmark)* **8**, 1424-1439 (2007).

14. Loehr, J.A. *et al.* NADPH oxidase mediates microtubule alterations and diaphragm dysfunction in dystrophic mice. *Elife* **7**, e31732 (2018).

15. Kerr, J.P. *et al.* Detyrosinated microtubules modulate mechanotransduction in heart and skeletal muscle. *Nature communications* **6**, 8526-8526 (2015).

16. Nelson, D.M. *et al.* Variable rescue of microtubule and physiological phenotypes in mdx muscle expressing different miniaturized dystrophins. *Human molecular genetics* **27**, 2090-2100 (2018).

17. Mackeh, R. *et al.* Reactive oxygen species, AMP-activated protein kinase, and the transcription cofactor p300 regulate α-tubulin acetyltransferase-1 (αTAT-1/MEC-17)-dependent microtubule hyperacetylation during cell stress. *J Biol Chem* **289**, 11816-11828 (2014).

18. Hać, A., Pierzynowska, K. & Herman-Antosiewicz, A. S6K1 Is Indispensible for Stress-Induced Microtubule Acetylation and Autophagic Flux. *Cells* **10**, 929 (2021).

19. Zheng, Z. *et al.* Histone deacetylase 6 inhibition restores autophagic flux to promote functional recovery after spinal cord injury. *Experimental Neurology* **324**, 113138 (2020).

20. Matsuyama, A. *et al.* In vivo destabilization of dynamic microtubules by HDAC6-mediated deacetylation. *The EMBO journal* **21**, 6820-6831 (2002).

21. Seto, E. & Yoshida, M. Erasers of histone acetylation: the histone deacetylase enzymes. *Cold Spring Harb Perspect Biol* **6**, a018713-a018713 (2014).

670 22. Bettica, P. *et al.* Histological effects of givinostat in boys with Duchenne muscular dystrophy.
671   *Neuromuscular disorders : NMD* **26**, 643-649 (2016).
672 23. Hubbert, C. *et al.* HDAC6 is a microtubule-associated deacetylase. *Nature* **417**, 455-458 (2002).
673 24. Choi, H. *et al.* Increased acetylation of Peroxiredoxin1 by HDAC6 inhibition leads to recovery of
674   Aβ-induced impaired axonal transport. *Molecular Neurodegeneration* **12**, 23 (2017).
675 25. Parmigiani, R.B. *et al.* HDAC6 is a specific deacetylase of peroxiredoxins and is involved in redox
676   regulation. *Proceedings of the National Academy of Sciences* **105**, 9633-9638 (2008).
677 26. Cosenza, M. & Pozzi, S. The Therapeutic Strategy of HDAC6 Inhibitors in Lymphoproliferative
678   Disease. *Int J Mol Sci* **19**, 2337 (2018).
679 27. Guedes-Dias, P. *et al.* HDAC6 inhibition induces mitochondrial fusion, autophagic flux and
680   reduces diffuse mutant huntingtin in striatal neurons. *Biochimica et Biophysica Acta (BBA) -*
681   *Molecular Basis of Disease* **1852**, 2484-2493 (2015).
682 28. Yan, S. *et al.* Pharmacological Inhibition of HDAC6 Attenuates NLRP3 Inflammatory Response
683   and Protects Dopaminergic Neurons in Experimental Models of Parkinson's Disease. *Frontiers in*
684   *Aging Neuroscience* **12** (2020).
685 29. Jian, W. *et al.* Inhibition of HDAC6 increases acetylation of peroxiredoxin1/2 and ameliorates 6-
686   OHDA induced dopaminergic injury. *Neuroscience Letters* **658**, 114-120 (2017).
687 30. Song, R. *et al.* HDAC6 inhibition protects cardiomyocytes against doxorubicin-induced acute
688   damage by improving α-tubulin acetylation. *Journal of molecular and cellular cardiology* **124**, 58-
689   69 (2018).
690 31. Saito, S. *et al.* Tubastatin ameliorates pulmonary fibrosis by targeting the TGFβ-PI3K-Akt
691   pathway. *PloS one* **12**, e0186615 (2017).
692 32. Leng, Y. *et al.* Inhibition of HDAC6 Activity Alleviates Myocardial Ischemia/Reperfusion Injury in
693   Diabetic Rats: Potential Role of Peroxiredoxin 1 Acetylation and Redox Regulation. *Oxidative*
694   *Medicine and Cellular Longevity* **2018**, 9494052 (2018).
695 33. Shen, Z. *et al.* Inhibition of HDAC6 by Tubastatin A reduces chondrocyte oxidative stress in
696   chondrocytes and ameliorates mouse osteoarthritis by activating autophagy. *Aging (Albany NY)*
697   **13**, 9820-9837 (2021).
698 34. Shi, Y. *et al.* Inhibition of HDAC6 protects against rhabdomyolysis-induced acute kidney injury.
699   *American Journal of Physiology-Renal Physiology* **312**, F502-F515 (2017).
700 35. Tsuboyama, K. *et al.* The ATG conjugation systems are important for degradation of the inner
701   autophagosomal membrane. *Science* **354**, 1036-1041 (2016).
702 36. Menon, M.B. & Dhamija, S. Beclin 1 Phosphorylation – at the Center of Autophagy Regulation.
703   *Frontiers in Cell and Developmental Biology* **6** (2018).
704 37. Geeraert, C. *et al.* Starvation-induced hyperacetylation of tubulin is required for the stimulation
705   of autophagy by nutrient deprivation. *J Biol Chem* **285**, 24184-24194 (2010).
706 38. Wang, Y. *et al.* SNARE-mediated membrane fusion in autophagy. *Semin Cell Dev Biol* **60**, 97-104
707   (2016).
708 39. Shen, Q. *et al.* Acetylation of STX17 (syntaxin 17) controls autophagosome maturation.
709   *Autophagy* **17**, 1157-1169 (2021).
710 40. Köchl, R., Hu, X.W., Chan, E.Y. & Tooze, S.A. Microtubules facilitate autophagosome formation
711   and fusion of autophagosomes with endosomes. *Traffic (Copenhagen, Denmark)* **7**, 129-145
712   (2006).
713 41. Xie, R., Nguyen, S., McKeehan, W.L. & Liu, L. Acetylated microtubules are required for fusion of
714   autophagosomes with lysosomes. *BMC Cell Biol* **11**, 89 (2010).
715 42. Akella, J.S. *et al.* MEC-17 is an α-tubulin acetyltransferase. *Nature* **467**, 218-222 (2010).
716 43. Verhey, K.J. & Hammond, J.W. Traffic control: regulation of kinesin motors. *Nature reviews.*
717   *Molecular cell biology* **10**, 765-777 (2009).

28

44. Hirokawa, N. & Takemura, R. Molecular motors and mechanisms of directional transport in neurons. *Nature reviews. Neuroscience* **6**, 201-214 (2005).

45. Reagan-Shaw, S., Nihal, M. & Ahmad, N. Dose translation from animal to human studies revisited. *FASEB journal : official publication of the Federation of American Societies for Experimental Biology* **22**, 659-661 (2008).

46. Olthoff, J.T. *et al.* Loss of peroxiredoxin-2 exacerbates eccentric contraction-induced force loss in dystrophin-deficient muscle. *Nature Communications* **9**, 5104 (2018).

47. Rhee, S.G. Overview on Peroxiredoxin. *Molecules and cells* **39**, 1-5 (2016).

48. Stoughton, W.B., Li, J., Balog-Alvarez, C. & Kornegay, J.N. Impaired autophagy correlates with golden retriever muscular dystrophy phenotype. *Muscle & nerve* **58**, 418-426 (2018).

49. Iannotti, F.A. *et al.* Effects of non-euphoric plant cannabinoids on muscle quality and performance of dystrophic mdx mice. *Br J Pharmacol* **176**, 1568-1584 (2019).

50. Whitehead, N.P. Enhanced autophagy as a potential mechanism for the improved physiological function by simvastatin in muscular dystrophy. *Autophagy* **12**, 705-706 (2016).

51. Segatto, M. *et al.* BETs inhibition attenuates oxidative stress and preserves muscle integrity in Duchenne muscular dystrophy. *Nat Commun* **11**, 6108 (2020).

52. Nowosad, A. *et al.* p27 controls autophagic vesicle trafficking in glucose-deprived cells via the regulation of ATAT1-mediated microtubule acetylation. *Cell Death & Disease* **12**, 481 (2021).

53. Nemazanyy, I. *et al.* Defects of Vps15 in skeletal muscles lead to autophagic vacuolar myopathy and lysosomal disease. *EMBO molecular medicine* **5**, 870-890 (2013).

54. Nascimbeni, A.C., Fanin, M., Angelini, C. & Sandri, M. Autophagy dysregulation in Danon disease. *Cell Death & Disease* **8**, e2565-e2565 (2018).

55. Wei, Y., Pattingre, S., Sinha, S., Bassik, M. & Levine, B. JNK1-mediated phosphorylation of Bcl-2 regulates starvation-induced autophagy. *Mol Cell* **30**, 678-688 (2008).

56. Guo, B. *et al.* O-GlcNAc-modification of SNAP-29 regulates autophagosome maturation. *Nature Cell Biology* **16**, 1215-1226 (2014).

57. Cheng, X. *et al.* Pacer Is a Mediator of mTORC1 and GSK3-TIP60 Signaling in Regulation of Autophagosome Maturation and Lipid Metabolism. *Mol Cell* **73**, 788-802.e787 (2019).

58. Belanto, J.J. *et al.* Independent variability of microtubule perturbations associated with dystrophinopathy. *Human molecular genetics* **25**, 4951-4961 (2016).

59. Fass, E., Shvets, E., Degani, I., Hirschberg, K. & Elazar, Z. Microtubules support production of starvation-induced autophagosomes but not their targeting and fusion with lysosomes. *J Biol Chem* **281**, 36303-36316 (2006).

60. Liu, J. *et al.* Key Role of Microtubule and Its Acetylation in a Zinc Oxide Nanoparticle-Mediated Lysosome-Autophagy System. *Small (Weinheim an der Bergstrasse, Germany)* **15**, e1901073 (2019).

61. Ittner, L.M., Ke, Y.D. & Götz, J. Phosphorylated Tau interacts with c-Jun N-terminal kinase-interacting protein 1 (JIP1) in Alzheimer disease. *The Journal of biological chemistry* **284**, 20909-20916 (2009).

62. Seigneurin-Berny, D. *et al.* Identification of components of the murine histone deacetylase 6 complex: link between acetylation and ubiquitination signaling pathways. *Molecular and cellular biology* **21**, 8035-8044 (2001).

63. Batchu, S.N., Brijmohan, A.S. & Advani, A. The therapeutic hope for HDAC6 inhibitors in malignancy and chronic disease. *Clinical science* **130**, 987-1003 (2016).

64. Butler, K.V. *et al.* Rational Design and Simple Chemistry Yield a Superior, Neuroprotective HDAC6 Inhibitor, Tubastatin A. *Journal of the American Chemical Society* **132**, 10842-10846 (2010).

65. Maday, S. & Holzbaur, Erika L.F. Autophagosome Biogenesis in Primary Neurons Follows an Ordered and Spatially Regulated Pathway. *Developmental Cell* **30**, 71-85 (2014).

29

766   66.   Willmann, R. *et al.* Enhancing translation: guidelines for standard pre-clinical experiments in
767   mdx mice. *Neuromuscular disorders : NMD* **22**, 43-49 (2012).
768   67.   Millay, D.P. *et al.* Calcium influx is sufficient to induce muscular dystrophy through a TRPC-
769   dependent mechanism. *Proc Natl Acad Sci U S A* **106**, 19023-19028 (2009).

770

771

772

773

774

775

776

777

778

779

780

781

782

783

784

785

786

791   **Author Contributions:** A.A. and G.G.R conceived and design the experiments; A.A. performed

792   the experiments, analyzed data and wrote the manuscript; E.L.C. and G.G.R. performed ex-vivo

793   muscle contractility experiments; C.L.C. performed stretch induce ROS experiment; B.A.C

794   processed co-localization data. G.G.R. edited the final manuscript. All authors reviewed, edited

795   and approved the final version of manuscript.

796   **Competing Financial Interest:** The authors declare no competing financial interest

797   **Material and Correspondence-** Correspondence to George G Rodney (Rodney@bcm.edu)

798

799

800

801

802

803

804

805

806

31

807 **Table 1. Recovery Index for Tubastatin A treatment of mdx.**

Outcome Measures	Recovery Score by TubA (70mg /kg b.w. for 2 weeks) in *mdx* mice
Serum Creatine phosphokinase (CPK)	133.8%
Immune Infiltration (CD68$^+$ cells)	63.10%
Centralized nuclei	52.2%
Apoptotic cell death	92.14%
EDL ECC force production at 10th contraction	46.68%
Diaphragm Isometric force production (200Hz)	53.24%
Grip Strength normalized with Body weight	113.29%

808

809

810

811

812

813

814

815

816

32

Figure Legends

Fig. 1 Impaired autophagosomal biogenesis/maturation in *mdx* mice (a-b) Immunoblot and densitometry analysis for autophagy regulatory proteins involved in vesicle nucleation (n=6 per group) and (ATG14L; WT, n = 6; *mdx*, n = 5). **(c)** Skeletal muscle tissue lysate prepared and subjected to immunoprecipitation using anti-Beclin, and the associated ATG14L, and Bcl-2 were determined using immunoblotting (n=3 per group). **(d-e)** JIP-1/JNK signaling was detected by immunoblot with antibodies as indicated (n = 6 per group) and (p-Bcl-2; WT, n=6; *mdx*,n=5). Densitometry analysis of immunoblots represented by box plots**. (f-g)** Immunoblot for proteins involved in autophagosome maturation and elongation (WT, n = 6; *mdx*, n = 5). Densitometry analysis of immunoblot represented by graph. GAPDH served as a loading control. Statistical difference between two groups were determined using two-sample student-*t*-test and Welch's correction test was performed for non-equal variance between two groups.

Fig. 2 Impairment in the SNARE complex-mediated autophagosomal-lysosomal fusion in *mdx* mice (a-b) Protein expressions of SNARE tertiary complex-STX17, VAMP8, and SNAP29 was determined by immunoblot (WT, n = 6; *mdx*, n = 5). Densitometry analysis of immunoblot represented by box plots. **(c)** Skeletal muscle lysate was prepared and subjected to immunoprecipitation using anti-SNAP29, and the associated SNAP29, STX17, ATG14L, and VAMP8 were determined using immunoblotting (n=3 per group). GAPDH served as a loading control. Statistical difference between two groups were determined using two-sample student-*t*-test and Welch's correction test was performed for non-equal variance between two groups.

Fig. 3 Genetic ablation of p47^{phox} promotes autophagosomal maturation in *mdx* mice (a) Skeletal muscle lysate was prepared from muscles of WT, *mdx* and p47$^{-/-}$-*mdx* mice and subjected to immunoprecipitation using anti-Beclin, and the associated ATG14L, and Bcl-2 were determined using immunoblotting. Immunoblot for WT and *mdx* group are the same as shown in **Fig.1c**. **(b-c)** Immunoblot for JIP-1/JNK signaling proteins which participates in vesicle nucleation. Densitometry analysis of western blots represented by box plots **(d-e)** Protein expressions of autophagosome elongation marker, ATG5-12 was determined by western blot. Densitometry analysis of western blot represented by box plots. **(f)** Skeletal muscle tissue lysate was prepared from muscles of WT, *mdx* and p47$^{-/-}$-*mdx* mice and subjected to immunoprecipitation using anti-SNAP29, and the associated SNAP29, STX17, ATG14L, and VAMP8 were determined using immunoblotting. Immunoblot for WT and *mdx* group are the same as shown in **Fig.2c. (g-h)** Immunoblots of lysosomal proteins, LAMP2 and Cathepsin-B. Densitometry analysis of western blot represented by box plots. GAPDH served as a loading control. (*n*=3 per group in all the figure panels). Statistical difference between groups were determined using ANOVA with Tukey's *post hoc* test.

Fig.4. Altered tubulin-acetylation in *mdx* muscle (a-b) Protein expressions of α-tubulin, acetylated-α-tubulin, HDAC6 were determined by western blot (n=6 per group). Densitometry analysis of immunoblot represented by box plots. **(c-d)** Protein expressions of MTs motor proteins, kinesin-1 complex (KIF5B, KLC) and dynein were determined by western blotting. WT and *mdx* mice (n=6 per group). Densitometry analysis of immunoblot represented by box plots **(e)** Skeletal muscle tissue lysate was prepared and subjected to immunoprecipitation using anti-JIP-1, and the associated KIF5B, KLC, and JNK were determined using immunoblotting (n=3 per group). **(f-g)**

33

860   Protein expressions of α-tubulin, acetylated-α-tubulin, HDAC6 were determined by western blot in
861   *mdx* and p47$^{-/-}$/*mdx* mice (n=3 per group).   GAPDH as a loading control. Statistical difference
862   between two groups were determined using two-sample student-*t*-test.

863   **Fig. 5 HDAC6 inhibition promotes tubulin acetylation and recovers autophagic flux in *mdx***
864   **mice (a-b)** Protein expressions of α-tubulin, acetylated-α-tubulin, detyrosinated-α-tubulin, and
865   HDAC6 were determined by western blot in WT, *mdx* and TubA treated *mdx* mice (n=3 per group).
866   Densitometry analysis of immunoblot represented by box plots. **(c-d)** Immunoblot for autophagy
867   related proteins- p62 and LC3 (n = 3 per group). Densitometry analysis of western blots
868   represented by box plots. **(e)** Skeletal muscle lysate was prepared and subjected to
869   immunoprecipitation using anti-SNAP29, and the associated, STX17, ATG14L, and VAMP8 were
870   determined using immunoblotting (n=3 per group). **(f-g)** Representative immunofluorescence
871   micrograph of anti-SNAP29 labeled with secondary antibody *Alexa Fluor 594 (Red) and* anti-
872   VAMP8 labeled with secondary antibody *Alexa Fluor 488 (Green)*, counterstained with DAPI
873   *(nuclear stain)* from section of gastrocnemius (GAS) muscle from WT (n=3), *mdx (n=3)* and TubA
874   treated *mdx (n=5)(scale bar -50μm; Magnification-40X).*Quantitative values for colocalization
875   analysis was represented as the Pearson's Correlation Coefficient of SNAP29-VAMP8. **(h-i)**
876   Protein expressions of lysosomal proteins, LAMP2 (n=3 per group) and Cathepsin-B ((n=6 per
877   group) were determined by western blot in WT, *mdx,* and TubA treated *mdx* mice. Densitometry
878   analysis of western blots represented by box plots. GAPDH served as a loading control. Statistical
879   difference between groups were determined using ANOVA with Tukey'*s post hoc* test.

880   **Fig. 6 HDAC6 inhibition prevents deacetylation and hyperoxidation of PrxII in *mdx* mice (a)**
881   Skeletal muscle lysate was prepared and subjected to immunoprecipitation using anti-PrxII, and
882   the acetylation levels of PrxII was determined with the anti-acetyl lysine antibodies **(b-c)** Protein
883   expressions of total PrxII and Prx-SO$_{2/3}$ were determined by western blot in WT, *mdx,* TubA
884   treated *mdx* mice (n=3 per group). Densitometry analysis of western blots and the ratio of PrxSO$_{2/3}$
885   and total PrxII were represented by box plots. **(d)** Stretch-induced ROS measurements in
886   diaphragm muscles of *mdx (n=2)* and TubA treated *mdx (n=3)* mice. GAPDH served as a loading
887   control. Statistical difference between groups were determined using ANOVA with Tukey'*s post*
888   *hoc* test. . Statistical difference between two groups were determined using two-sample student-*t*-
889   test and Welch's correction test was performed for non-equal variance between two groups in
890   **panel d.**

891   **Fig.7. TubA treatment alleviates apoptosis and immune cells infiltration in *mdx* muscle. (a-**
892   **b)** Protein expressions of pro-caspase-3 and cleaved caspase-3 were determined by western blot
893   from TA muscles extract of WT, *mdx*, and TubA treated *mdx* (n = 3 per group). Densitometry
894   analysis of immunoblots represented by graph. GAPDH as a loading control **(c-d)** Paraffin-
895   embedded gastrocnemius (GAS) muscle sections (4μm) of WT (n=3), *mdx (n=3)* and *mdx*+TubA
896   (n=5) mice processed for the detection of TUNEL positive nuclei *(green).* Sections were stained
897   with α-laminin *(red)* to define the sarcolemma. Nuclei were counterstained with DAPI *(blue).*
898   White boxed region shows the enlarged image from the *mdx* muscle section in the panel on right
899   indicating TUNEL positive nuclei *(white arrow).*Numbers of TUNEL positive nuclei counted by
900   Image J software. **(e-f)** Macrophage infiltration analyzed by Immunofluorescence staining of
901   CD68 *(green)*, α-laminin *(red)*, and nuclei *(blue)* in GAS section isolated from WT (n=3), mdx
902   (n=3), *mdx*+TubA (n=5) mice. White boxed region shows the enlarged image from the *mdx* muscle
903   section indicating infiltration of CD68+ cells in the skeletal muscles *(white arrow).*Quantification

904 of CD68 positive immune cells. *Scale bar (50μm), Magnification-40X*. Statistical difference
905 between groups were determined using ANOVA with Tukey's *post hoc* test.

906 **Fig. 8 HDAC6 inhibition ameliorates muscle pathophysiology and improves muscle function**
907 **(a)** Serum creatine phosphokinase quantitated by ELISA (n = 8 per group) **(b-c)** Loss of
908 sarcolemmal integrity was evaluated by the *i.p*. Injection of Evans Blue Dye (EBD) in mice. Dye
909 injected 24hr prior to the completion of two weeks TubA treatment. EBD staining of diaphragm
910 (DIA) muscles and its cross section (4μm) showing EBD positive fibers. Quantification of EBD
911 positive fibers in DIA muscle fibers (n=3 per group). *Scale bar (90μm), Magnification-20X.* **(d)**
912 H&E-stained muscle (TA). White arrow head= peripheral nuclei; black arrow head=central nuclei;
913 black arrow=necrotic myofibers (infiltration of immune cells); black asterisk=fat depositions
914 within myofibers. (n = 3 mice per group), *Scale bar: 50 μm, Magnification-40X*.
915 Immunofluorescence staining of α-laminin (*green)* and DAPI (*blue nuclei staining*) in TA cross-
916 section muscle of WT, *mdx*, TubA treated *mdx*. (n=3 per group) (e) Percentage fibers with
917 centralized nuclei was quantified by Image J. *Scale bar: 50 μm, Magnification-40X* **(f)** Myofibers
918 CSA calculated from minimum feret's diameter (n=3 per group). **(g-h)** Grip strength, absolute and
919 normalized to body weight (n = 5 per group). **(i)** Force–frequency relationship in DIA muscle strips
920 from WT (n = 9), *mdx* (n = 8), and *mdx*+TubA (n = 9). **(j).** Eccentric contraction induced force
921 drop (normalized to the first contraction) in EDL muscles isolated from WT (n=6), *mdx (n=7)*,
922 TubA treated *mdx (n=6)* mice**.** Statistical difference between groups were determined using
923 ANOVA with Tukey's *post hoc* test.*p<0.05 vs BL10, **P<0.01 vs BL10, ***p<0.001 vs BL10,
924 *P<0.05 vs mdx, **p<0.01 vs mdx for panel i and j.

925 **Fig. 9. Model of Impaired autophagy in mdx skeletal muscle are differentially regulated by**
926 **redox and acetylation modifications**. **(A)** Loss of dystrophin leads to increased HDAC6
927 expression and subsequent deacetylation of α-tubulin. Decreased α-tubulin acetylation inhibits
928 binding of the kinesin-/JIP-1 complex and subsequent transport of autophagosomes to lysosomes.
929 Decreased activation of JIP-1 results in decreased phosphorylation of JNK and Bcl-2, preventing the
930 dissociation of BECN1/Bcl-2 and sequestering BECN1 away from the PI3classIII complex
931 (ATG14L-Vps34-Vps15). The net result is impairment of phagophore nucleation. Decreased WIPI-
932 1 inhibits localization of ATG5-12/16L1 complex to the phagophore, leading to impaired
933 autophagosome maturation in mdx mice. SNARE associated proteins play a major role in
934 membrane-mediated events of autophagosome-lysosome fusion, another crucial step in autophagy
935 process. In mdx mice, reduced interaction of SNAP29 with STX17 and VAMP8 leads to the
936 inhibition of autophagosome-lysosome fusion. **(B)** Genetic inhibition of Nox-2 activity in mdx
937 mice activates JIP-1, resulting in phosphorylation of JNK and Bcl-2, dissociation of BECN1 from
938 Bcl-2 and induction of phagophore nucleation. In addition, Nox-2 inhibition promotes ATG5-12
939 complex formation and therefore autophagosome maturation. However, autophagosome-lysosome
940 fusion is not improved upon inhibition of Nox-2 activity, likely due to no change in α-tubulin
941 acetylation. Pharmacological inhibition of HDAC6 promotes α-tubulin acetylation and improves
942 SNARE complex formation, thereby facilitating fusion of autophagosomes with lysosomes,
943 improves autophagy, decreases dystropathology and improves skeletal muscle function. Increased
944 acetylation of the antioxidant enzyme Prx II likely contributes to improved muscle function in mdx
945 skeletal muscle. **Figure created with BioRender.com**

Figure 1

Figure 2

a

b

c

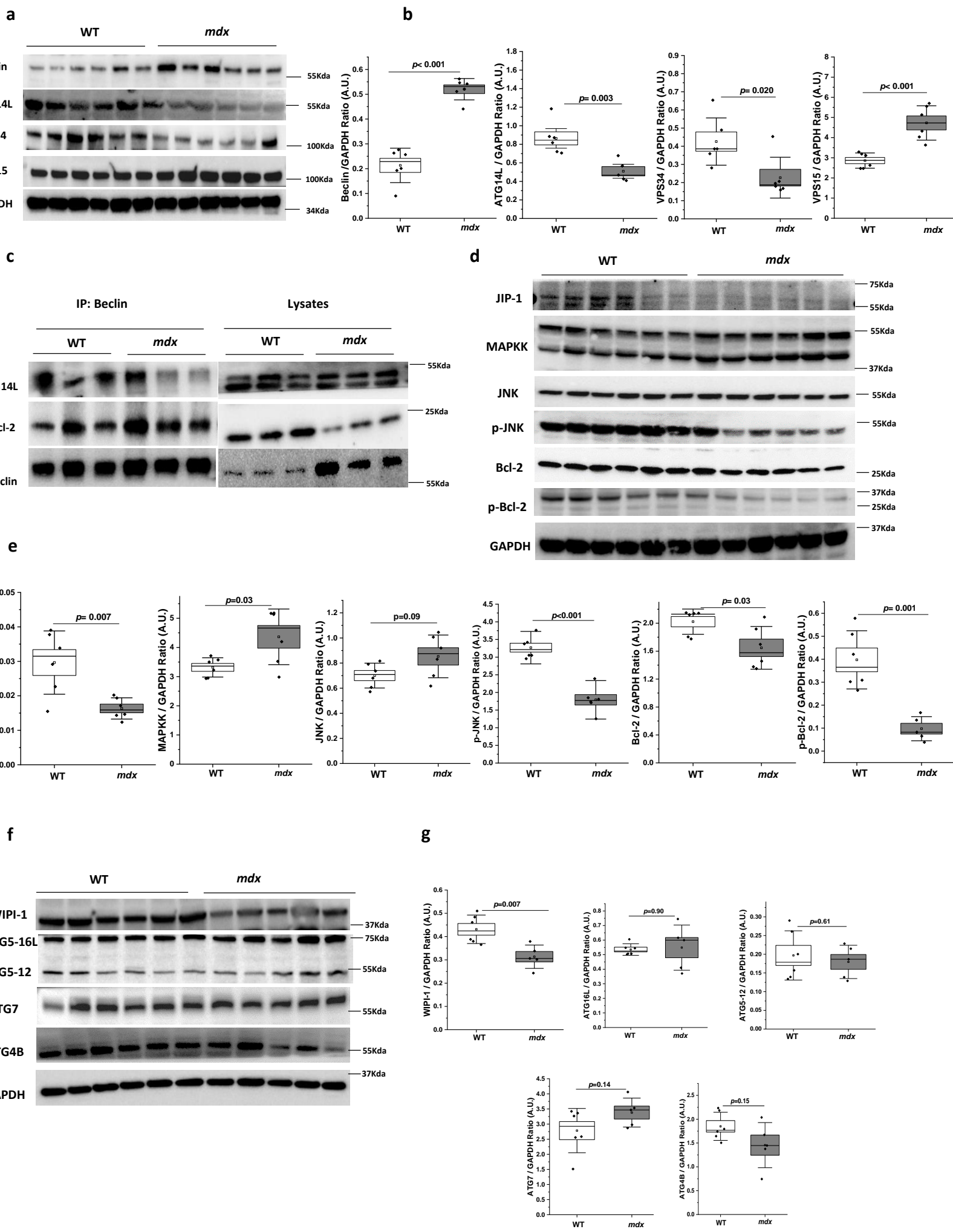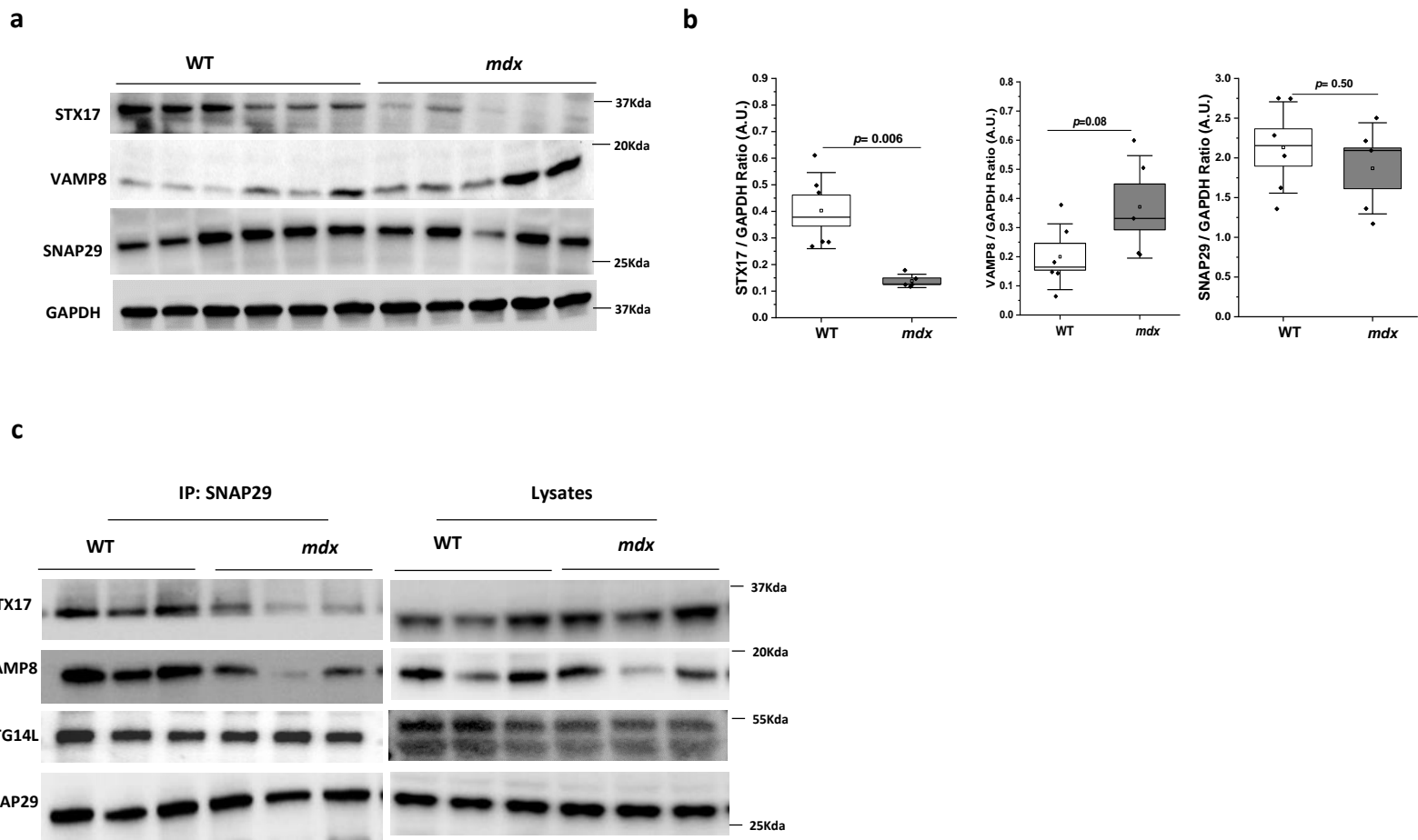**Figure 3**

Figure 4

Figure 5
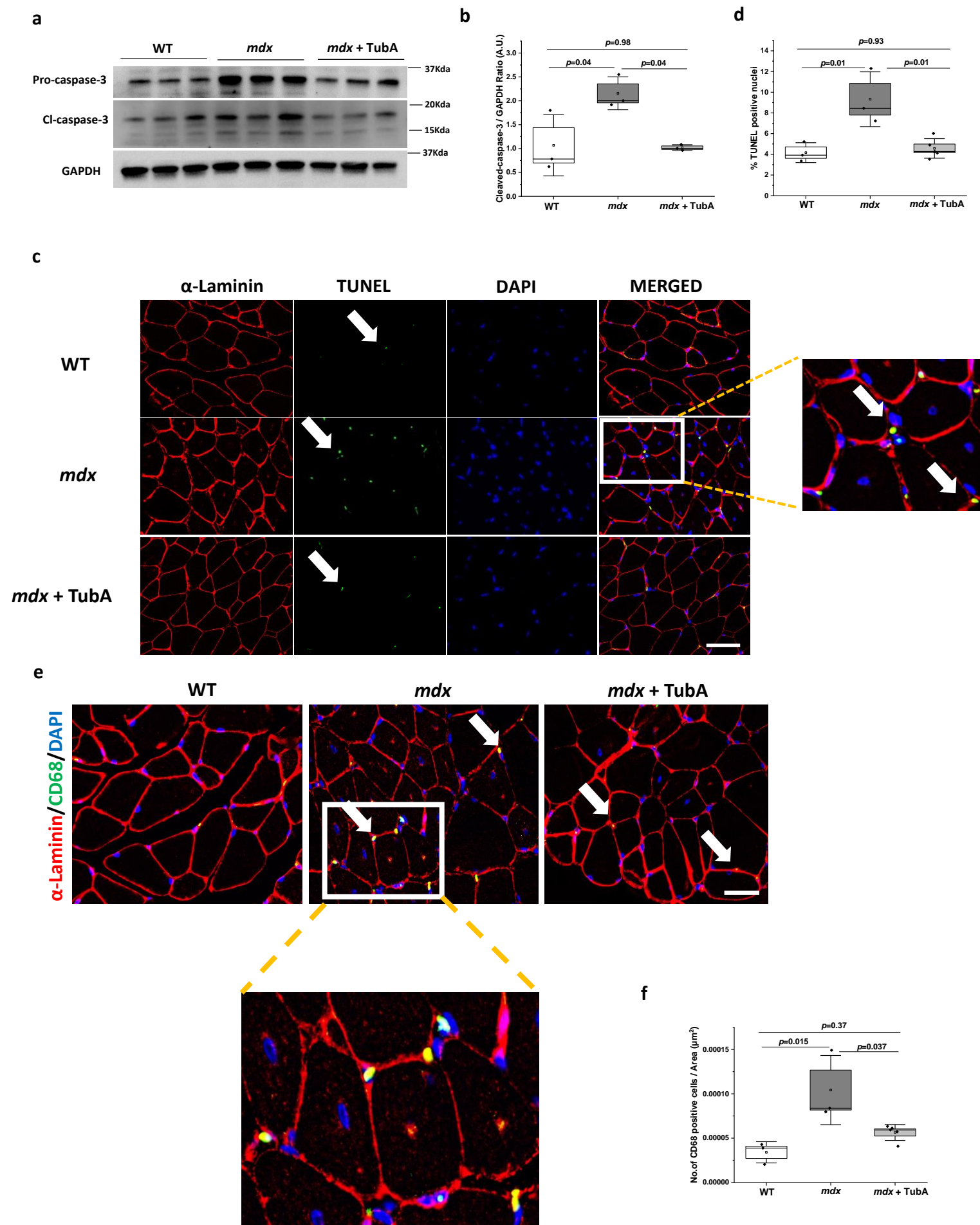
Figure 6

a

b

c
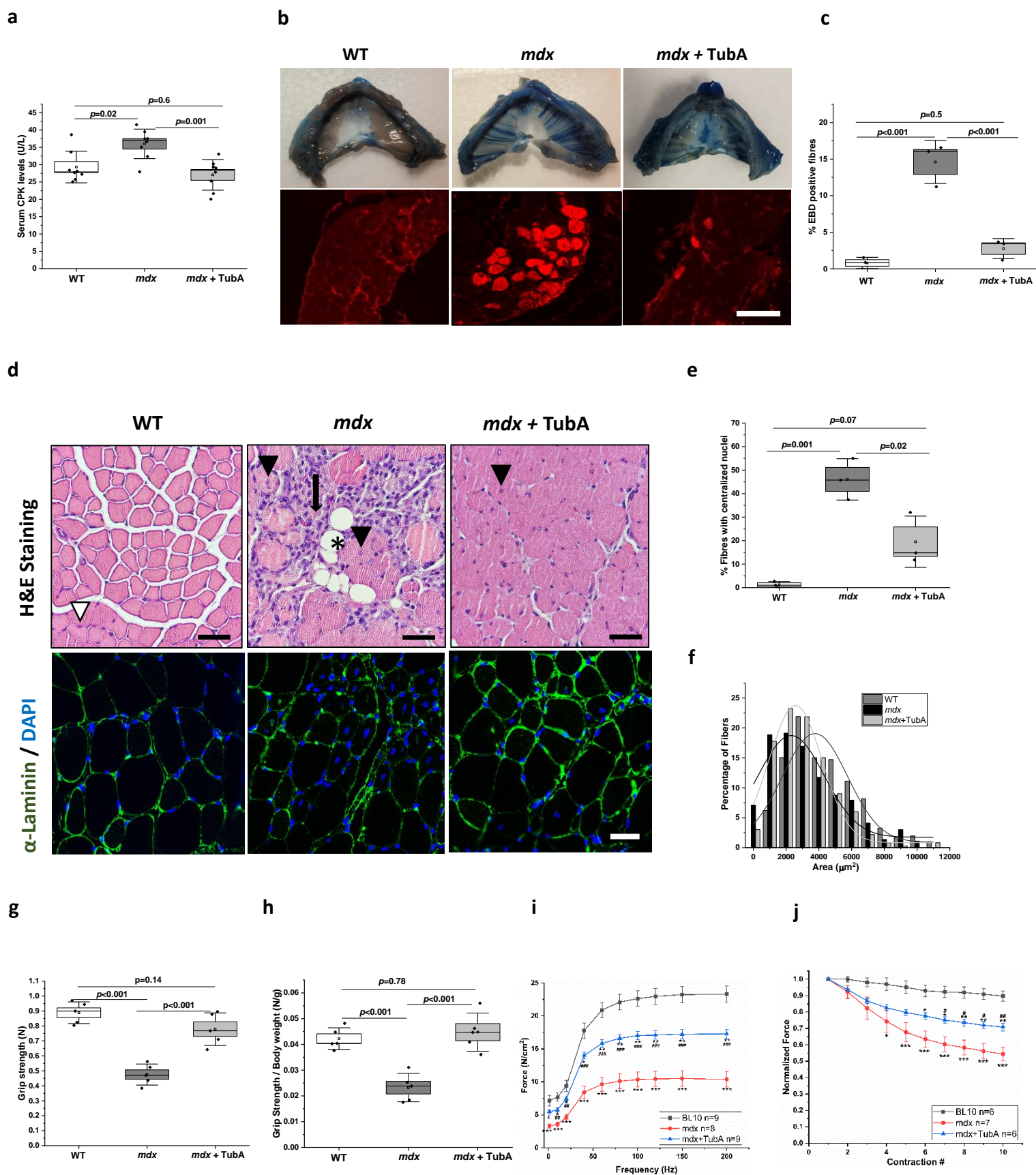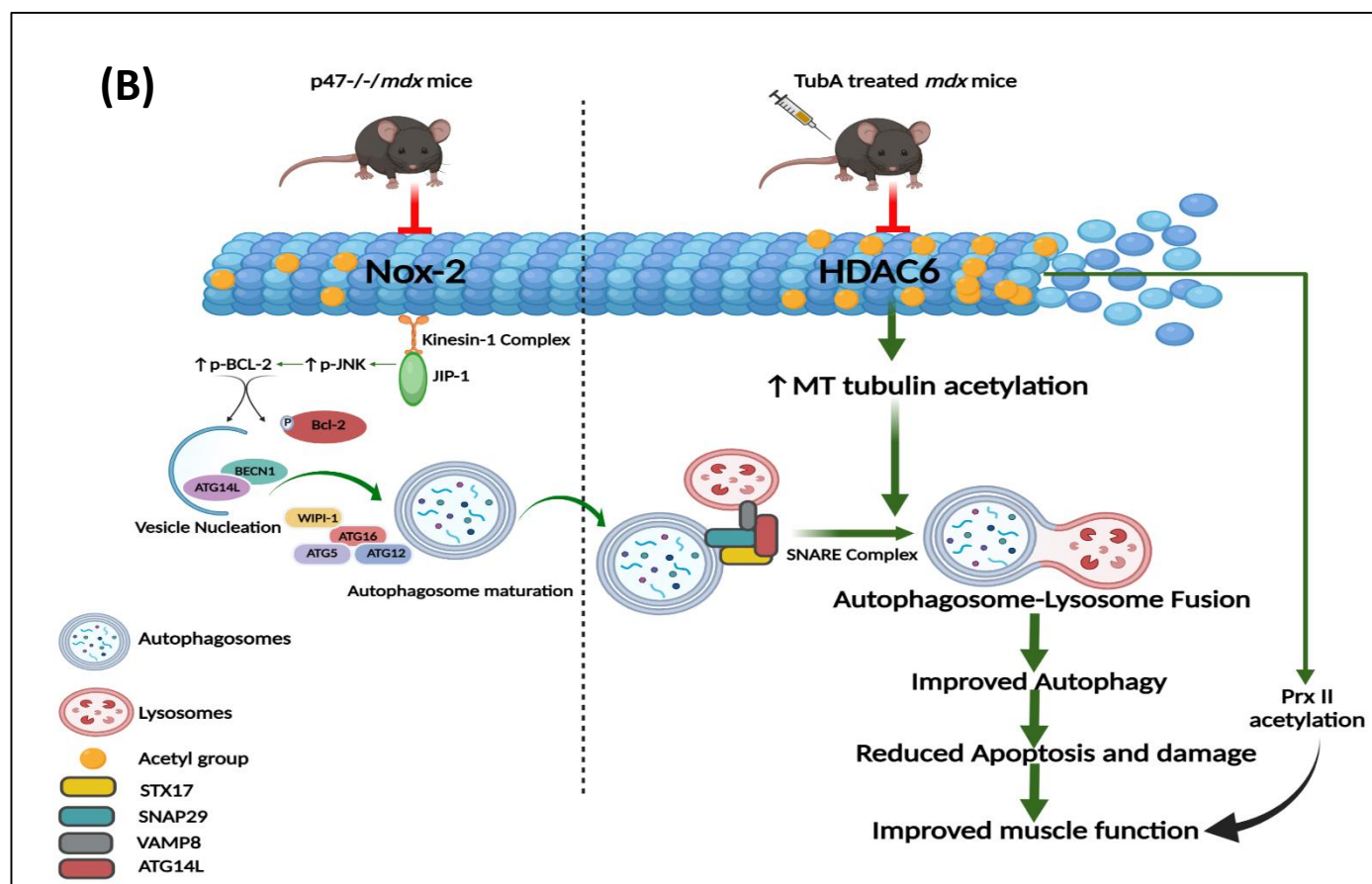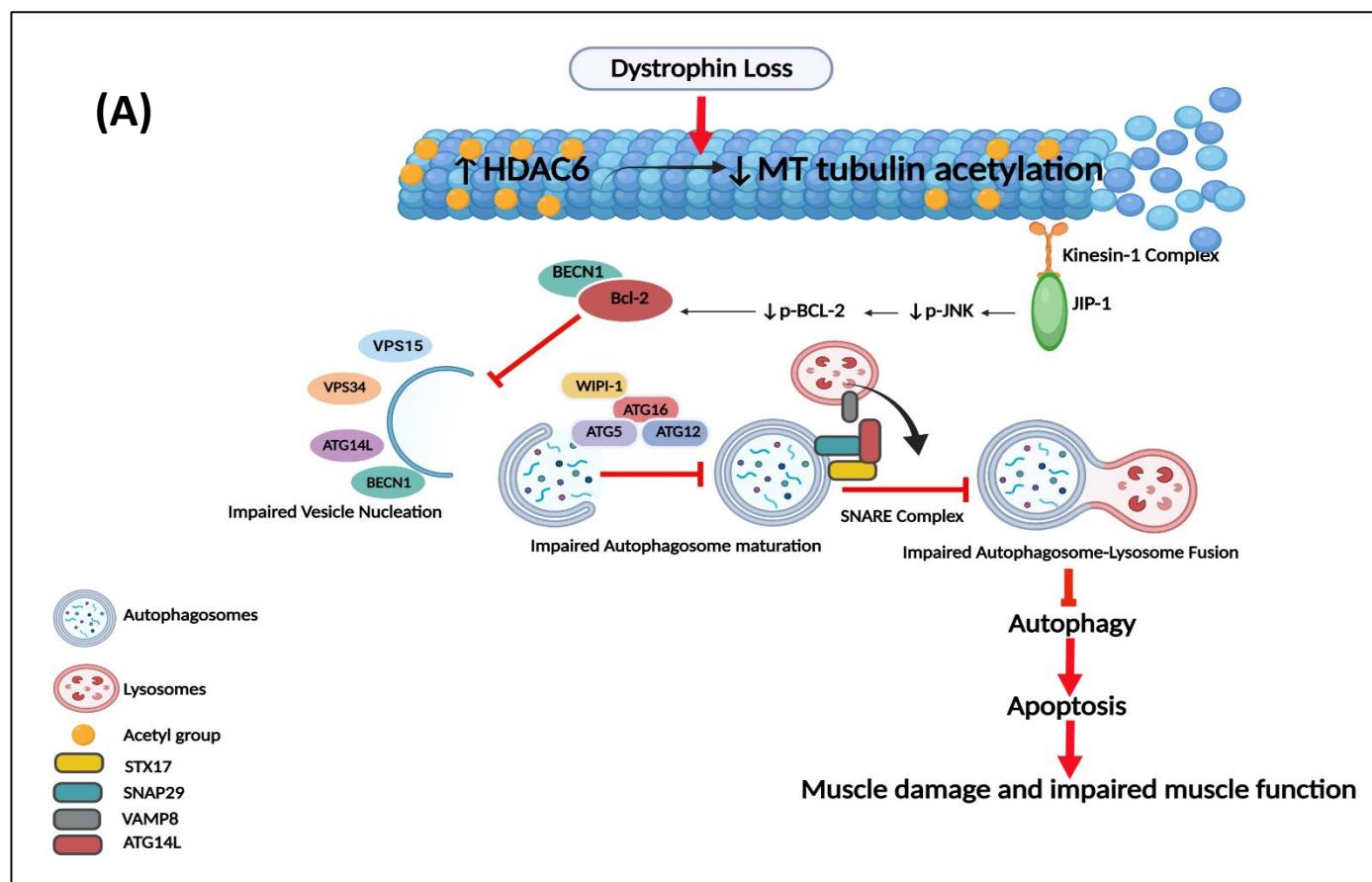

d
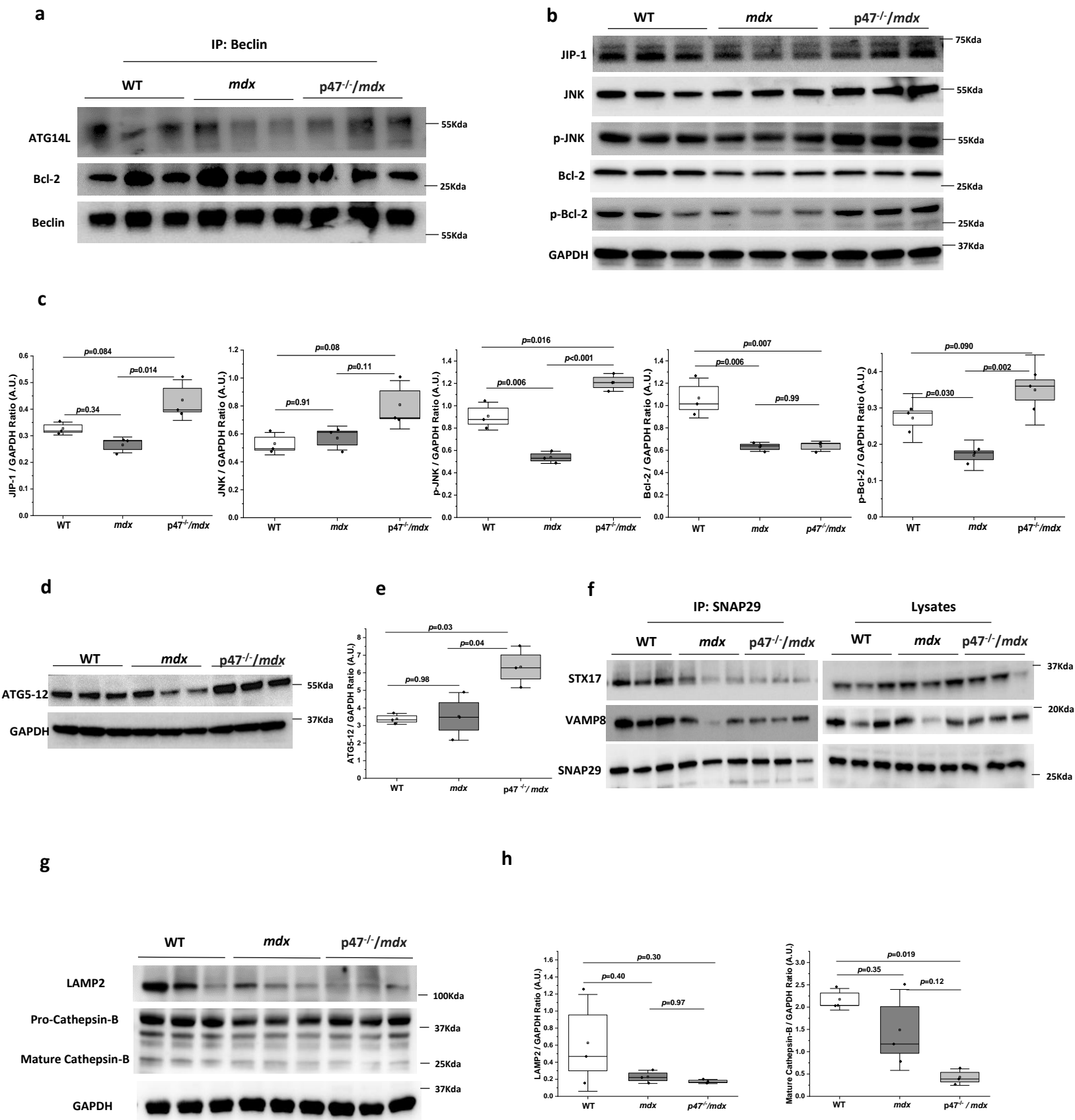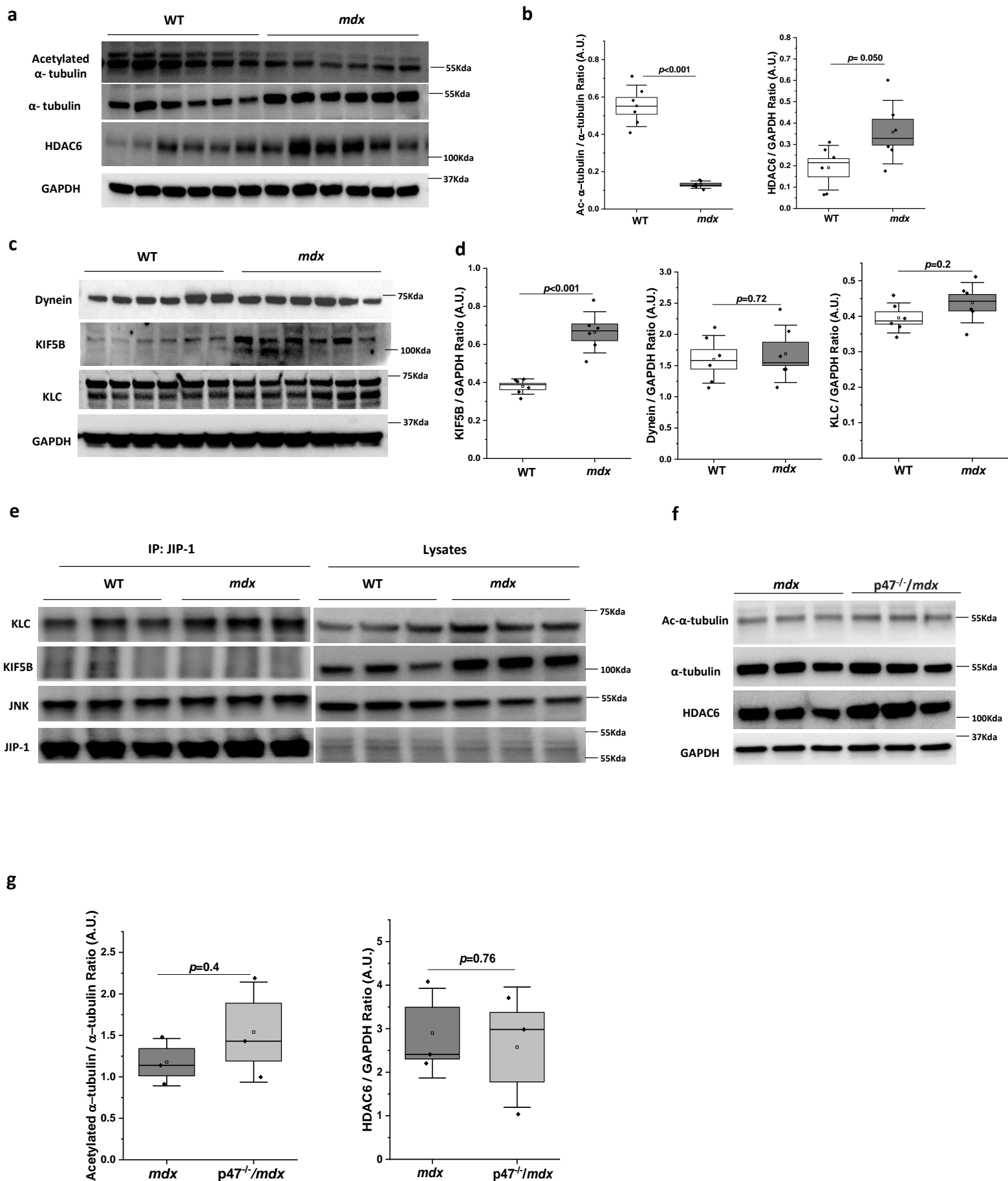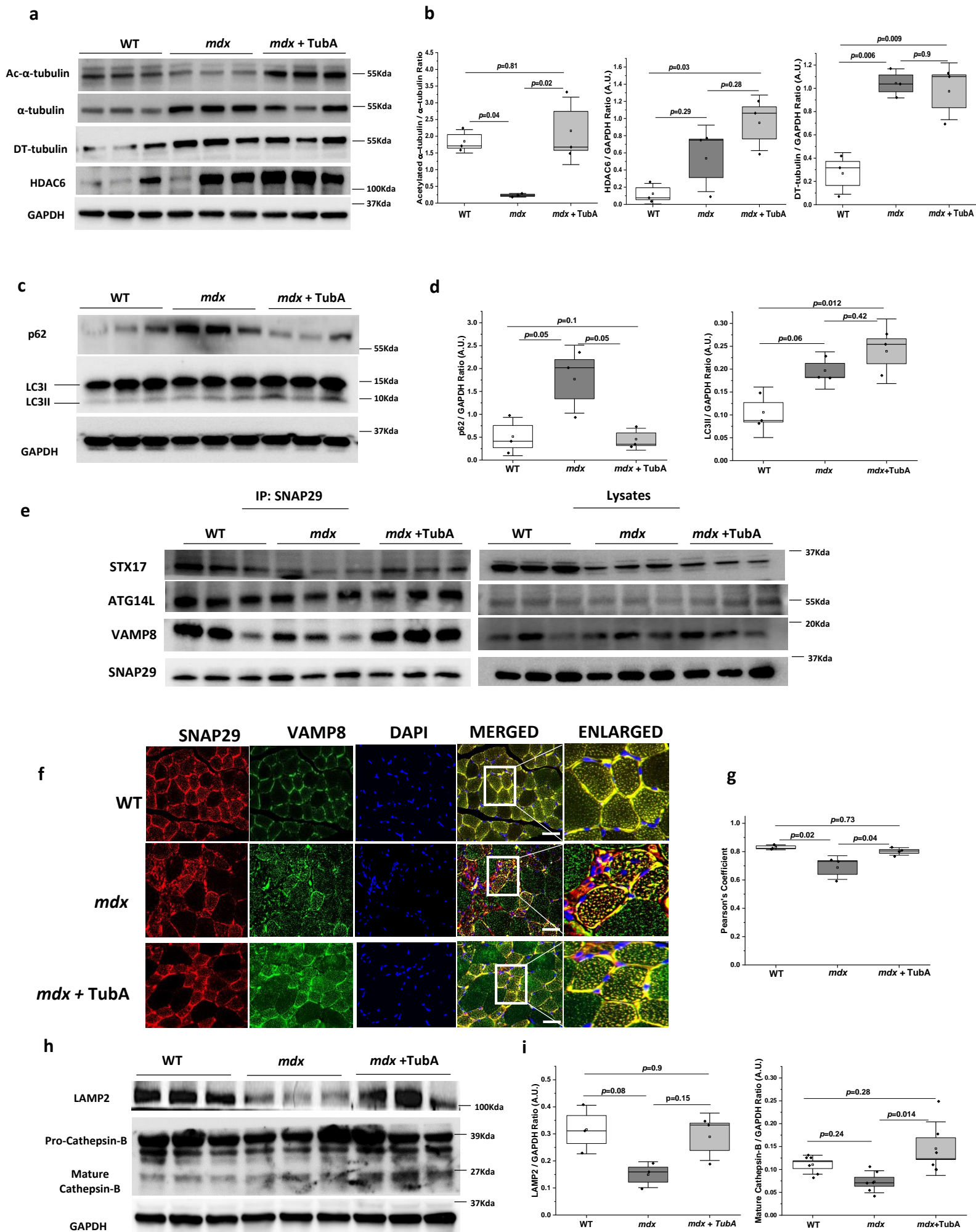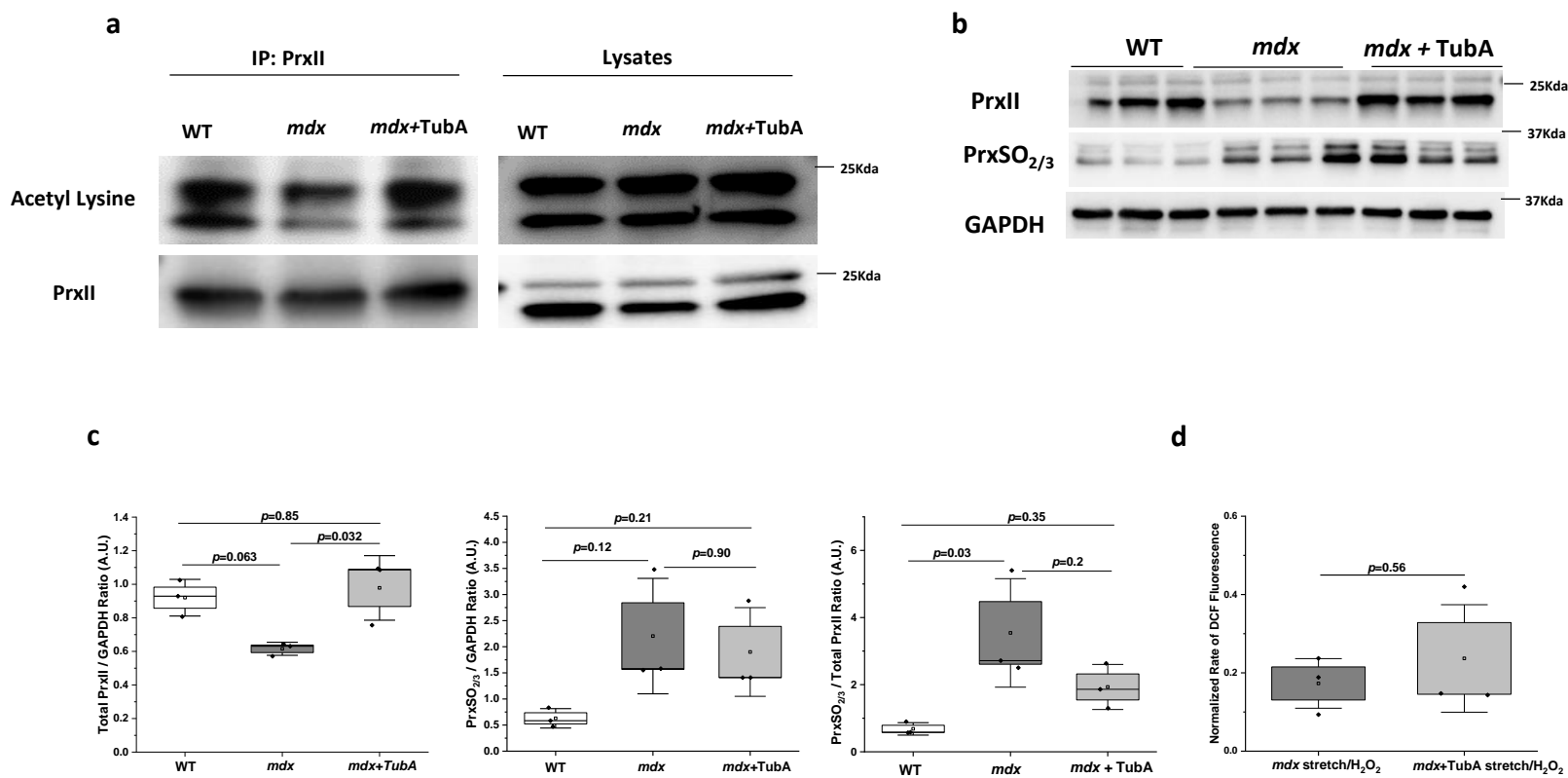
Figure 7

Figure 8

Figure 9

Histone deacetylase 6 inhibition promotes microtubule acetylation and facilitates autophagosome-lysosome fusion in dystrophin-deficient *mdx* mice

Akanksha Agrawal[1], Erin L. Clayton[1], Courtney L. Cavazos[1], Benjamin A. Clayton[1],

George G. Rodney[1*]

1. Department of Integrative Physiology, Baylor College of Medicine, Houston, TX, USA

*All correspondence should be sent to rodney@bcm.edu
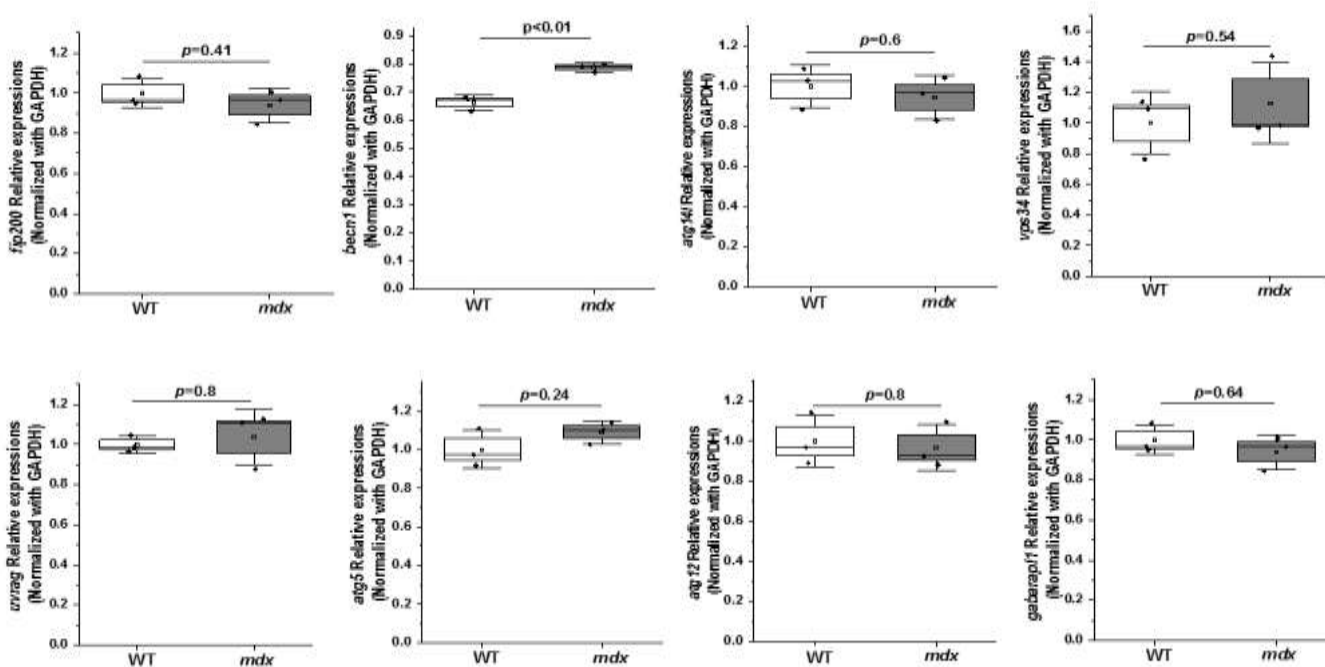
Supplementary Figure S1

Fig.S1. Gene expressional analysis of autophagy regulatory markers by Reverse-transcriptase PCR Graph represents relative gene expressions of *fip200, becn1, atg14l, vps34, uvrag, atg5, atg12, gabarapl1* normalized with GAPDH (n=3 per group). Statistical difference between two groups were determined using two-sample student-*t*-test.
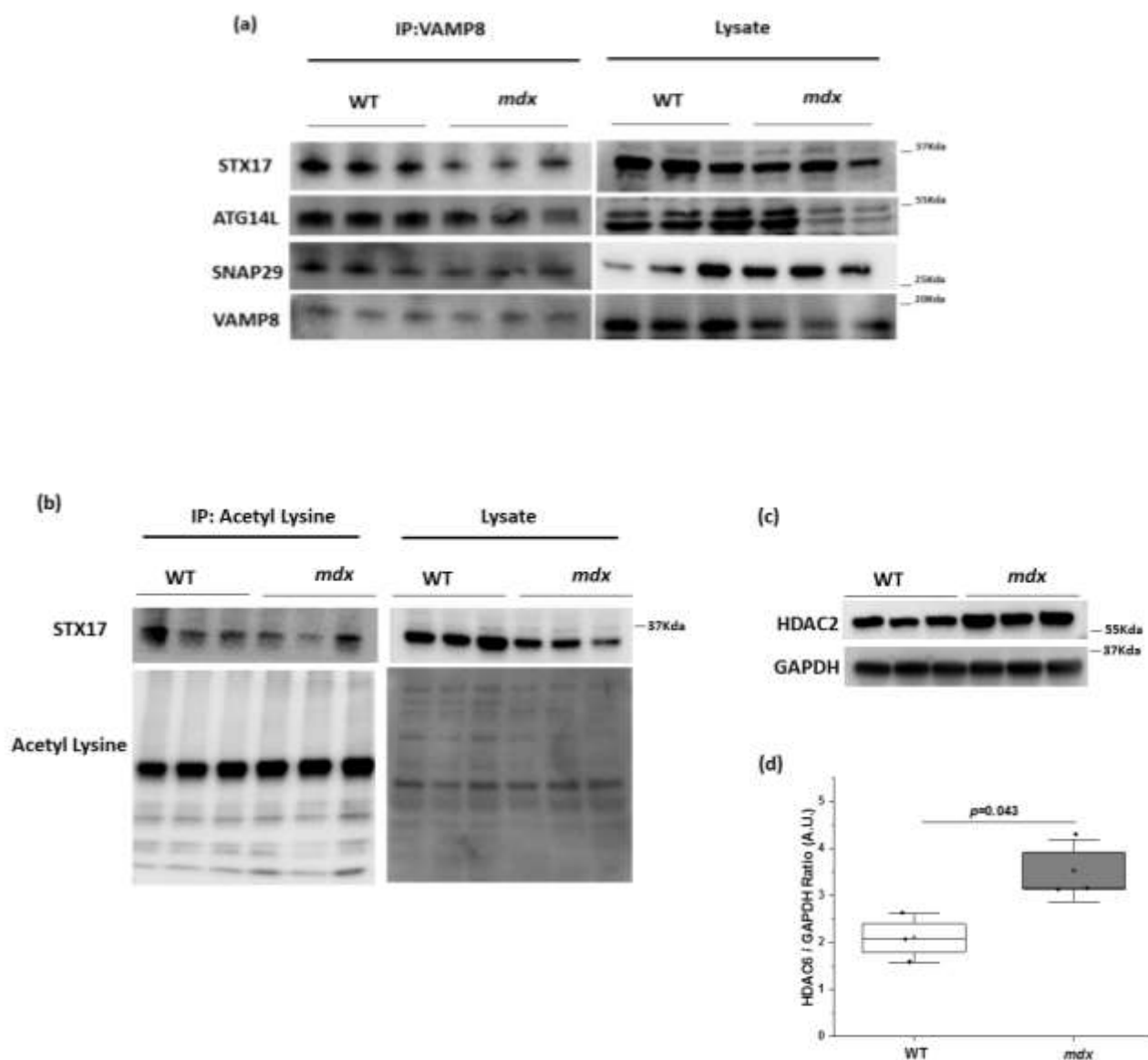
Supplementary Figure S2

Fig.S2. **Impaired autophagosome-lysosome fusion in *mdx* mice (a)** Skeletal muscle lysate was prepared and subjected to immunoprecipitation using anti-VAMP8, and the associated STX17, ATG14L, and SNAP29 were determined using immunoblotting **(b)** Anti-acetyl-lysine was immunoprecipitated, and bound STX17 was detected by western blotting using anti-STX17 antibody **(c-d)** Immunoblot represents protein expressions of HDAC2. GAPDH served as a loading control. Densitometry analysis of immunoblot represented by graph. (n=3 per group in all Figure panels). Statistical difference between two groups were determined using two-sample student-*t*-test.
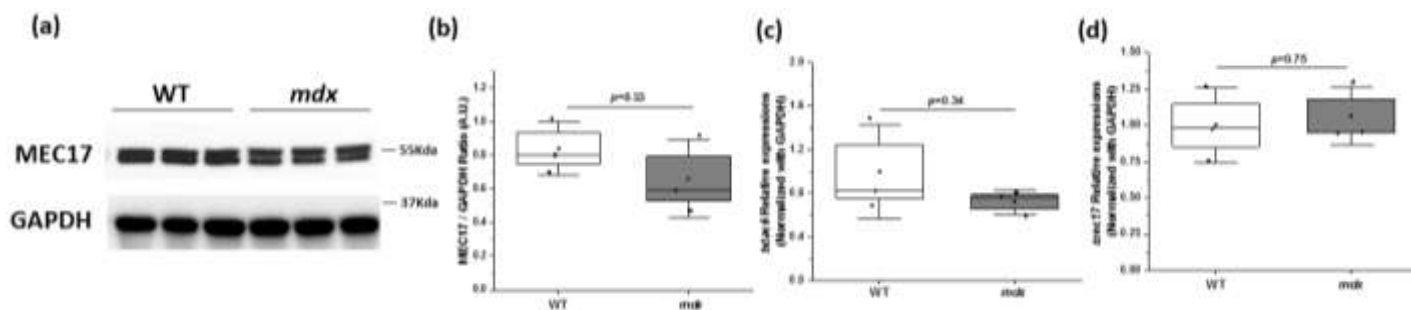
Supplementary Figure S3

Fig.S3. Expressional analysis of acetylase and deacetylase enzymes in *mdx* mice (a-b) Immunoblot represents protein expressions of MEC17. GAPDH served as a loading control. Densitometry analysis of immunoblot represented by graph **(c-d)** Graph represents relative gene expressions of deacetylase enzyme (*hdac6*) and acetylase enzyme (*mec17*) normalized with GAPDH. (n=3 per group in all Figure panels). Statistical difference between two groups were determined using two-sample student-*t*-test.
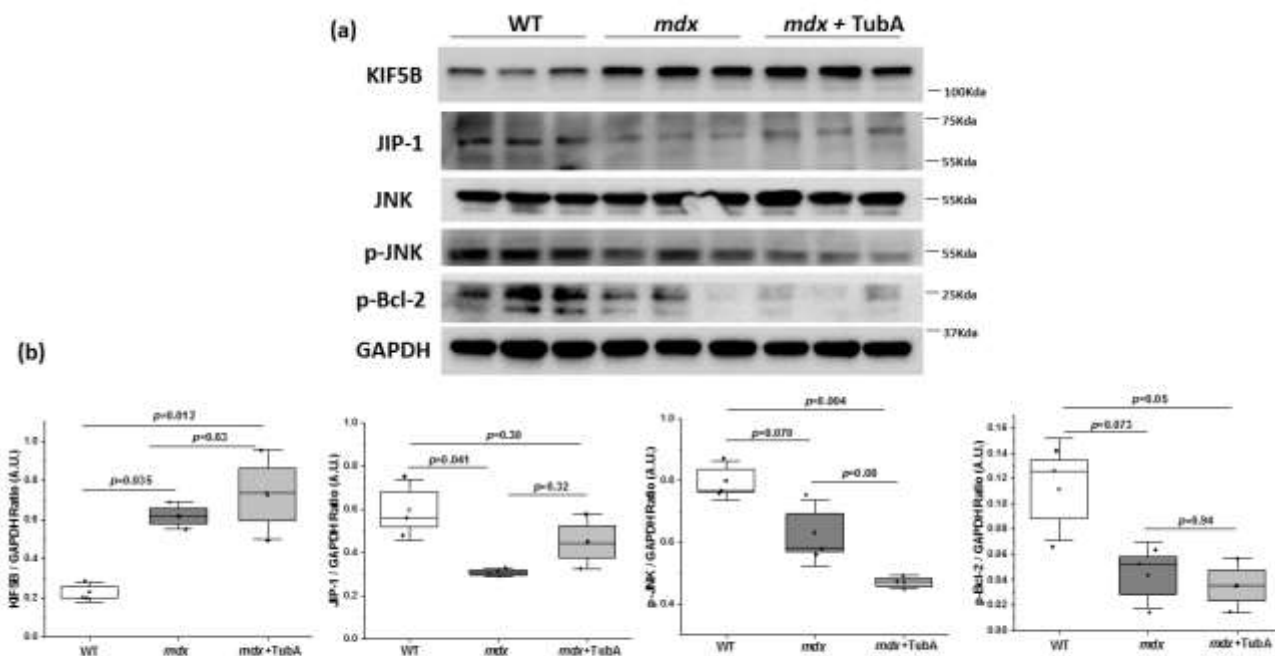
Supplementary Figure S4

Fig.S4 Effect of HDAC6 inhibition on Kinesin/JIP/JNK pathway in *mdx* mice (a-b) Protein expressions of Kinesin/JIP/JNK complex in WT, *mdx* and TubA treated *mdx* mice (n=3 per group). GAPDH served as a loading control. Densitometry analysis of immunoblot represented by graph. Statistical difference between groups were determined using ANOVA with Tukey's *post hoc* test.
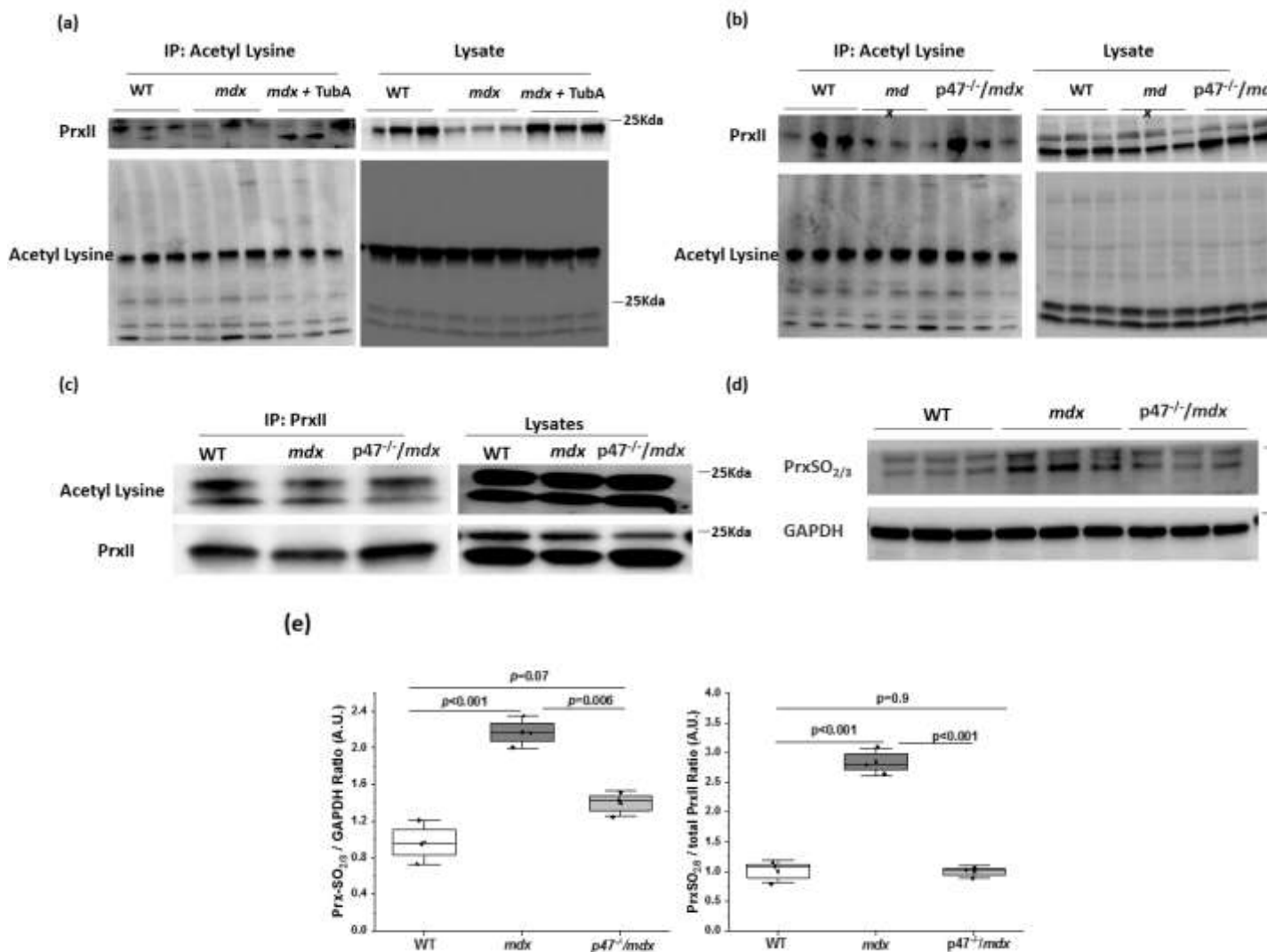
Supplementary Figure S5

Fig.S5. Acetylation status of PrxII in TubA treated *mdx* and genetically ablated Nox-2 *mdx* mice (a) Skeletal muscle lysate was prepared and subjected to immunoprecipitation using anti-acetyl-lysine, and the acetylation levels of PrxII was determined with the anti-PrxII antibodies in WT, *mdx*, and TubA treated *mdx* mice (n=3 per group). Input blot of PrxII for WT *mdx* and *mdx*+TubA group in Fig.S5a are the same as shown in **Fig.6b (b)** Immunoprecipitation was performed using anti-acetyl-lysine, and the acetylation levels of PrxII was determined with the anti-PrxII antibodies in WT, *mdx*, and p47 [-/-]/*mdx* mice (n=3 per group) **(c)** Immunoprecipitation was performed using anti-PrxII, and the acetylation levels of PrxII was determined with the anti-acetyl lysine antibodies in WT, *mdx*, and p47 [-/-]/*mdx* mice **(d-e)** Immunoblot represents hyperoxidation state of PrxII (PrxSO$_{2/3}$) in WT, *mdx*, and p47 [-/-]/*mdx* mice (n=3 per group). Densitometry analysis of western blots and the ratio of PrxSO$_{2/3}$ and total PrxII were represented by graph. GAPDH served as a loading control. Statistical difference between groups were determined using ANOVA with Tukey's *post hoc* test.
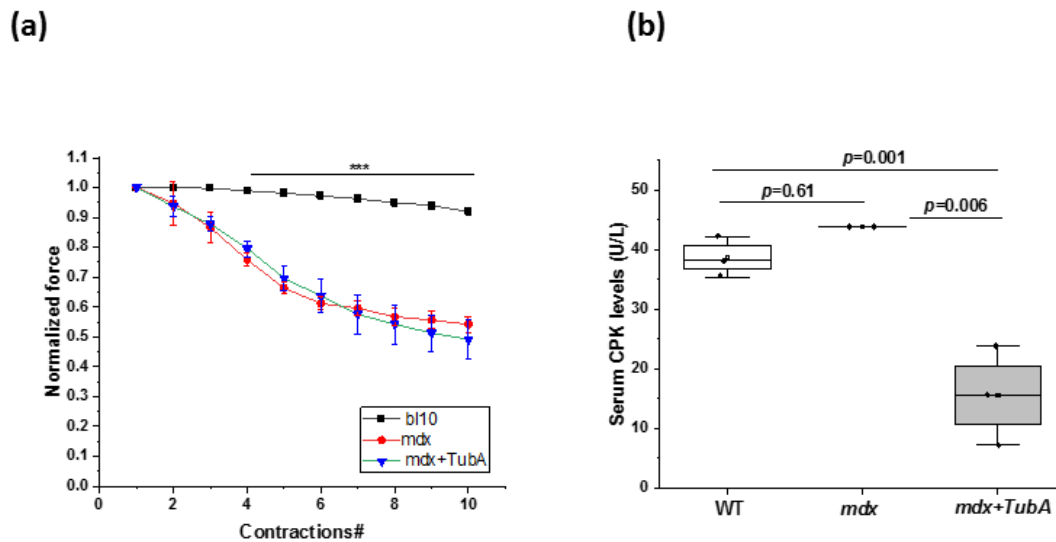
Supplementary Figure S6

Fig.S6 Effect of TubA on muscle contraction and damage at different dose and time point (a) HDAC6 specific inhibitor, TubA at 30mg/kg b.w. injected into mdx mice intraperitoneally for 4 weeks every other day. After completion, EDL muscle isolated from WT (n=2, *mdx (n=3)*, TubA treated *mdx (n=3)* mice and Eccentric contraction induced force drop (normalized to the first contraction) was performed. **(b)** Serum creatine kinase quantitate by ELISA from WT (n=3), *mdx (n=2)*, TubA treated *mdx (n=3)* mice. Statistical difference between groups were determined using ANOVA with Tukey'*s post hoc* test.***p<0.001 vs *mdx* and *mdx* +TubA for **panel a**.

Table S1: Supplementary Table 1 Primary Antibody dilutions

Primary Antibodies	Company/Catalogue No.	Dilution
Anti-Beclin-1	CST-3738S	**WB-1:1000 IP-1:50**
Anti-Bcl-2	Sigma-SAB4500003	**1:800**
Anti-ATG14L	Sigma-A6358	**1:1000**
Anti-VPS34	CST-3811	**1:1000**
Anti-VPS15	CST-14580S	**1:1000**
Anti-KIF5B	Abcam-ab167429	**1:800**
Anti-KLC	Abcam-ab187179	**1:1000**
Anti-Dynein	EMD Millipore corp-MAB1618	**1:1000**
Anti-JNK	CST-9252S	**1:1000**
Anti-p-JNK	CST-9251S	**1:1000**
Anti-p-Bcl-2	CST-2827S	**1:1000**
Anti-MAPKK	Sigma-M5795	**1:1000**
Anti-JIP-1	Sigma-SAB4503651	**WB-1:800 IP-1:50**
Anti-WIPI-1	Abcam-ab139722	**1:1000**
Anti-ATG7	CST-D12B11	**1:1000**
Anti-ATG4B	CST-5299S	**1:1000**
Anti-ATG5-12	CST-2630	**1:1000**
Anti-LC3	CST-83506	**1:1000**
Anti-P62	CST-5114S	**1:1000**
Anti-STX17	Abcam-ab229646	**1:800**
Anti-SNAP29	Abcam-ab181151	**WB-1:1000 IP-1:50**

Anti-VAMP8	Abcam-ab76021	**WB-1:1000 IF-1:100**
Anti-alpha-tubulin	CST-2144S	**1:1000**
Anti-Acetylated-alpha-tubulin	Sigma-T7461	**1:800**
Anti-HDAC6	CST-7621S	**1:1000**
Anti-MEC17/aTAT1	Thermo Fischer-PAS69188	**1:1000**
Anti-Detyrosinated alpha tubulin	Abcam-ab48389	**1:800**
Anti-CD68	Santa Cruz Biotechnologies, sc-20060	**IF-1:100**
Anti-PrxII	Sigma-R8656	**WB-1:1000 IP:50**
Anti-Prx-SO3	Abcam-ab16830	**1:800**
Anti-Acetyl Lysine	CST-9441S	**WB-1:1000 IP-1:50**
Anti-GAPDH	EMD Millipore Corp-MAB374	**1:10000**
Anti-Caspase-3	CST-9662S	**1:800**
Anti-LAMP2	Santa Cruz Biotechnologies ,sc-18822	**1:800**
Anti-Cathepsin-B	Santa Cruz Biotechnologies ,sc-365558	**1:800**
Anti-alpha-laminin	ab11575	**IF-1:100**
Anti-SNAP29	Santa Cruz Biotechnologies, sc-390602	**IF:100**

Table S2 Supplementary Table 2 Secondary Antibodies

Secondary antibodies	Company/catalogue	Dilution
Anti-mouse	Sigma-GENA931	1:10000
Anti-rabbit	Sigma-GENA934	1:10000
Alexa-fluor 594 donkey anti-rabbit	Invitrogen A21207	1:1000
Alexa –Fluor-488-donkey anti-rabbit	Invitrogen A21206	1:1000
Alexa-Fluor-594-goat anti-mouse	Invitrogen A11032	1:1000